Mon. Not. R. Astron. Soc. **387,** 1627–1648 (2008) doi:10.1111/j.1365-2966.2008.13342.x

A study of X-ray flares – I. Active late-type dwarfs

J. C. Pandey★† and K. P. Singh★
Tata Institute of Fundamental Research, Mumbai 400 005, India

Accepted 2008 April 16. Received 2008 April 4; in original form 2007 August 22

ABSTRACT

We present temporal and spectral characteristics of X-ray flares observed from six late-type G–K active dwarfs (V368 Cep, XI Boo, IM Vir, V471 Tau, CC Eri and EP Eri) using data from observations with the *XMM–Newton* observatory. All the stars were found to be flaring frequently and altogether a total of 17 flares were detected above the 'quiescent' state X-ray emission which varied from 0.5 to 8.3 $\times$ 10^{29} erg s^{-1}. The largest flare was observed in a low-activity dwarf XI Boo with a decay time of 10 ks and ratio of peak flare luminosity to 'quiescent' state luminosity of 2. We have studied the spectral changes during the flares by using colour–colour diagram and by detailed spectral analysis during the temporal evolution of the flares. The exponential decay of the X-ray light curves, and time evolution of the plasma temperature and emission measure are similar to those observed in compact solar flares. We have derived the semiloop lengths of flares based on the hydrodynamic flare model. The size of the flaring loops is found to be less than the stellar radius. The hydrodynamic flare decay analysis indicates the presence of sustained heating during the decay of most flares.

Key words: stars: activity – stars: coronae – stars: flare – stars: late-type – X-rays: stars.

1 INTRODUCTION

Flares are events in which a large amount of energy is released in a short interval of time. Such events take place at almost all frequencies of the electromagnetic spectrum and have been observed in the Sun as well as in many types of cool stars (Garcia-Alvarez et al. 2002). These stellar flares could be radiating several orders of magnitude more energy than a solar flare. Optical flares in UV Cet (dMe) type stars are a common phenomenon. The flares produced by other stellar sources (e.g. RS CVn and BY Dra) are usually detected only in the ultraviolet (UV) or X-rays. These UV and X-ray flares show extreme luminosities and very hot temperatures ($\gtrsim$10 MK). Even though, flares in these stars present many analogies with the solar flares, there are also significant differences, such as the amount of energy released. A general model for stellar flares has emerged from numerous solar flare studies (Güdel 2004). The flare reconnection region, located somewhere at large coronal heights, primarily accelerates electrons and ions up to MeV energy (Dennis & Schwartz 1989). The accelerated electrons participate along the magnetic fields into chromosphere where they heat the cool plasma to coronal flare temperatures, thus evaporating a part of the chromosphere into the corona. Early X-ray observations with the *EXOSAT* observatory of flare stars revealed examples of two different type of flares: (1) impulsive flares which are like compact solar flares, and (2) long decay flares which are like two-ribbon solar flares (Pallavicini, Tagliaferri & Stella 1990). The compact flares are less energetic ($\sim 10^{30}$ erg s^{-1}), short in duration ($<$1 h) and confined to a single loop while the long decay flares are more energetic ($\sim 10^{32}$ erg s^{-1}), of long duration ($\geqslant$1 h) and release the energy in an entire arcade of loops (Garcia-Alvarez 2000). The most likely flare process relates to an opening up of magnetic fields and subsequent relaxation by closing the open field lines.

Analysis of light curves during flares can provide us with insights into the characteristics of the coronal structures and, therefore, of the magnetic field (e.g. Schimtt & Favata 1999; Favata, Micela & Reale 2000b; Reale et al. 2004). Even though stellar flares are spatially unresolved, a great deal of information on the coronal heating and on the plasma structure morphology can be inferred from a detailed modelling of stellar flares; for instance, if sufficient data are available for moderately time-resolved spectral analysis, a study of the complete evolution of a flare can allow us to (a) infer whether the flare occurs in closed coronal structures (loops), (b) determine the size of the flaring structures, (c) determine whether continuous heating is present throughout the flare and (d) put constraints on the location and distribution of the heating (see Reale et al. 2004).

Active solar-type (G–K) dwarfs are known to possess magnetic fields on their surfaces, and the field strengths are as large as several kilogauss, i.e. stronger than the strongest field observed on the Sun (e.g. Saar 1990; Johns-Krull & Valenti 1996). Cyclic behaviour has been identified in several late-type active stars (Baliunas et al. 1995; Olah & Strassmeier 2002), suggesting that dynamos similar to the solar dynamos are also operative in solar-type stars. These

★E-mail: jeewan@aries.ernet.in (JCP); singh@tifr.res.in (KPS)
†Present address: Aryabhatta Research Institute of Observational Sciences, Nainital 263 129, India.

Table 1. General properties of stars in the sample.

Name	Spectral type	V (mag)	Period (d)	Distance (pc)
V368 Cep	G9V	7.54	2.74	19.7
XI Boo	G8V/K4V	4.55	6.2	6.6
IM VIR	G5V/KV	9.00	1.3086	60.0
V471 Tau	K2V/dW	9.71	0.52	46.7
CC Eri	K7Ve/M4V	8.76	1.56	11.5
EP ERI	K2V	6.00	6.85	10.3

solar-type stars are less active than the dMe stars (so-called flare stars). However, they show more frequent flaring activity than the late-type evolved stars (e.g. RS CVns; Güdel 2004). In this paper, we present analysis of archival data obtained from *XMM–Newton* Observations of six G–K dwarfs, namely V268 Cep, XI Boo, IM Vir, V471 Tau, EP Eri and CC Eri with the aim to understand the spectral and temporal characteristics of X-ray flares in them. In subsequent papers we will examine the characteristics of X-ray flares in the subgiants and the giants.

The paper is organized as follows: in Section 2 we give the basic parameters of stars in our sample, in Section 3 we describe the observational data sets that we have analysed and the methods of data reduction, Section 4 contains our analysis and results and in Section 5 we present our discussion and conclusions.

2 BASIC PARAMETERS OF SAMPLE STARS

The basic parameters of stars in our sample are given in Table 1. V368 Cep (= HD 220140; $V = 7.54$ mag) is a G9V spectral-type chromospherically active star with photometric period of 2.74 d (Chugainov, Lovkaya & Petrov 1991; Chugainov, Petrov & Lovkaya 1993). XI Boo (= HD 131156; $V = 4.55$ mag) is a nearby visual binary, comprising a primary G8 dwarf and a secondary K4 dwarf with an orbital period of 151 yr (Hoffleit & Jaschek 1982). In terms of the outer atmospheric emission, UV and X-ray observations show that the primary dominates entirely over the secondary (Hartmann et al. 1979; Ayres, Marstad & Linsky 1981; Schimtt 1997; Laming & Drake 1999). XI Boo (primary) is a slow rotator with rotation period of 6.2 d (Gray et al. 1996). A cool main-sequence eclipsing binary (G5V+KV), IM Vir (= HD 111487; $V = 9.69$ mag) has an orbital period of 1.31 d (Malkov et al. 2006). V471 Tau (= BD+16516; $V = 9.71$ mag) is a rapidly rotating detached eclipsing binary first observed by Nelson & Young (1970). The system is composed of a cool main-sequence chromospherically active K2 V star (Guinan & Sion 1984) and a degenerate hot white dwarf separated by 3.4 stellar radii. CC Eri (= HD 16157, $V = 8.8$ mag) is a spectroscopic binary with orbital period of 1.561 d. It consists of a K7Ve primary and a dM4 secondary, with mass ratio of $\sim$2 (Strassmeier et al. 1993). The primary star corotates with orbital motion due to the tidal lock, and is one of the fastest rotating K dwarfs in the solar neighbourhood. EP Eri (=HD 17925; $V = 6.0$ mag) is very nearby (10.3 pc), very young (high Li I abundances), active K2-type dwarf with a rotation period of 6.85 d (Cayrel de Strobel & Cayrel 1989; Cutispoto 1992; Henry, Fekel & Hall 1995). The presence of an unresolved companion in this star has been suggested by Henry et al. (1995) based on the variable widths of the photospheric absorption lines reported in the literature ($v \sin i$ ranges from 3 to 8 km s^{-1}; see Fekel 1997).

3 OBSERVATIONS AND DATA REDUCTION

The late-type dwarf stars in our sample were observed with the *XMM–Newton* satellite using varying detector set-ups. The *XMM–Newton* satellite is composed of three co-aligned X-ray telescopes (Jansen et al. 2001) which observe a source simultaneously, accumulating photons in three CCD-based instruments: the twin MOS1 and MOS2 and the PN (Strüder et al. 2001; Turner et al. 2001), all three detectors constituting the EPIC (European Photon Imaging Camera) camera. The EPIC instrument consists of three CCD cameras with two different types of CCD, two MOS and one PN, providing the imaging and spectroscopy in the energy range from 0.15 to 15 keV with a good angular [point spread function (PSF) = 6 arcsec full width at half-maximum (FWHM)] and a moderate spectral resolution ($E/\Delta E \approx 20$–50). Exposure time for each star was in the range of 30–60 ks. A log of observations is provided in Table 2.

The data were reduced with standard *XMM–Newton* Science Analysis System (SAS) software, version 7.0 with updated calibration files (Ehle et al. 2004). The preliminary processing of raw EPIC Observation Data Files was done using the EPCHAIN and EMCHAIN tasks which allow calibration both in energy and astrometry of the events registered in each CCD chip and to combine them in a single data file for MOS and PN detectors. The background contribution is particularly relevant at high energies where coronal sources have very little flux and are often undetectable. Therefore, for further analysis we have selected the energy range between 0.3 and 10.0 keV. Event list file was extracted using the SAS task EVSELECT. The EPATPLOT task was used for checking the existence of pile-up affecting the inner region of all stars. Only the star CC Eri was found to be affected by pile-up. X-ray light curves and spectra of all target stars were generated from on-source counts obtained from circular regions with a radius $\sim$40–50 arcsec around each source. However, for the star CC Eri, X-ray light curves and spectra were extracted with events taken from an annulus of 32 arcsec with inner radius of 12 arcsec to avoid pile-up effect in the inner region. The background was taken from several source-free regions on the detectors at nearly the same offset as the source and surrounding the source.

4 ANALYSIS AND RESULTS

4.1 Multiband X-ray light curves and characterization of flares

The background subtracted X-ray light curves of six stars viz. V356 Cep, IM Vir, V471 Tau, CC Eri and EP Eri, as observed with the MOS and PN detectors are shown in Figs 1(a)–(f), respectively. All light curves are in the energy band 0.3–10.0 keV. The MOS and PN light curves are represented by solid and open circles, respectively. The temporal binning of light curves is 200 s for all sources. The PN light curve of the star IM Vir was affected by proton flares twice during the observations, first for 800 s after 10 ks from the beginning of the observation, and second at the end, after 40 ks of the observations. However, the MOS light curve was affected only at the end of the observation. For the star EP Eri, the high proton flare background region in the light curve is for a duration of 3 ks after 14.7 ks from the beginning of the observation. We have removed data during the proton flare background from the MOS and PN light curves of both the stars IM Vir and EP Eri. The star XI Boo was not observed by the PN detector, and only the light curve obtained with the MOS is presented here.

Table 2. Log of observations with the *XMM–Newton*.

Star name	Instrument (mode, filter)	Start time date (UT)	Exposure time (s)	Offset (arcmin)
V368 Cep	MOS1 (SW, thick)	2003 December 27 (19:23:43)	29 762	0.045
	MOS2 (SW, thick)	2003 December 27 (19:23:43)	29 768	
	PN (SW, thick)	2003 December 27 (19:28:55)	29 570	
XI Boo[a]	MOS1 (T, medium)	2001 January 19 (11:25:06)	58 397	0.150
	MOS2 (SW, medium)	2001 January 19 (11:25:06)	58 997	
IM VIR	MOS1 (FF, medium)	2004 July 15 (04:49:45)	53 488	9.093
	MOS2 (FF, medium)	2004 July 15 (04:49:45)	53 487	
	PN (FF, medium)	2004 July 15 (05:32:47)	51 077	
V471 Tau	MOS1 (LW, medium)	2004 August 1 (06:52:10)	60 678	1.052
	MOS2 (LW, medium)	2004 August 1 (06:52:10)	60 682	
	PN (SW, medium)	2004 August 1 (06:57:35)	60 471	
CC Eri	MOS1 (PFW, thick)	2003 August 8 (08:40:36)	39 463	0.065
	MOS2 (T, thick)	2003 August 8 (08:40:27)	39 212	
	PN (PFW, thick)	2003 August 8 (09:21:36)	36 703	
EP Eri	MOS1 (SW, thick)	2004 January 20 (17:53:18)	50 013	0.015
	MOS2 (SW, thick)	2004 January 20 (17:53:19)	50 013	
	PN (SW, thick)	2004 January 20 (17:58:29)	50 013	

[a]XI Boo was observed for 895 s by EPIC PN detector.
Note. FF: full frame; FPW: fullprime window; PPW: primepartial window;
SW: small window; T: timing; LW: large window.

The light curves of all the individual stars show variability on a time-scale of ks, most of which resembles flaring activity. The customary definition of a flare is a significant increase in intensity, after which the initial or quiescent level of intensity is reached again. Such patterns are observed in the light curves of the sample stars shown in Figs 1(a)–(f), and where the 'flare regions' are represented by arrows and marked by F*i*, where $i = 1, 2, \ldots, 17$ refers to the flare number. The mean quiescent level count rates of the sources are taken from regions that are free from flares and are marked by Q in the Fig. 1. The start time, end time, flare duration and flux during quiescent and at flare peak for all the 17 flares observed are listed in Table 3. The peak and quiescent state count rates as given in Table 3 are converted into flux by using the WebPIMMS,[1] where we assumed the plasma temperature of 1 keV. Flares F6, F7, F9, F14 and F16 were found to be long lasting ($\geqslant$2.3 h) flares. In fact, the flare F7 of the XI Boo is longest flare observed with total duration of $\sim$3.1 h. The peak flux in these long duration flares was found to be more than two times than the quiescent state. Other detected flares were shorter than 1.3 h. The shortest duration flare was detected one in V368 Cep (F3) and other in CC Eri (F12). In these short duration flares, peak X-ray flux was 1.3–1.8 times more than that of the quiescent state.

To characterize the flares, we have fitted the light curves of the flares with an exponential function

$$c(t) = A_0 \mathrm{e}^{-[(t-t_0)/\tau_\mathrm{d}]} + q, \quad (1)$$

where $c(t)$ is the count rate as a function of time t, t_0 is the time of peak count rate, q is the count rate in the quiescent state, τ_d is the decay time of the flare and A_0 is the count rate at flare peak. The best-fitting parameters for the flares are given in Table 4 for both the MOS and the PN data. For five flares, F6 and F7 of XI Boo, F9 of IM Vir, F14 of CC Eri and F16 of EP Eri, the e-fold decay time was found to be more than 1 h. Flare F7 of XI Boo was found to be the longest decay flare ($\tau_\mathrm{d} = 10$ ks) observed among all the 17 flares. The flare F16 shows a very different structure when compared to the other flares, i.e. a sharp rise and a highly structured decay as if more flares were present during the decay. Though it was tough to locate the peak of flare F16 because of its complex structure, the decay time was determined to be 4 ks. For the remaining 11 flares the decay time was found to be in the range of 8–47 min. The decay phase of the flare F17 was not observed. The rise times of all flares were found to be less than 1 h. The rise and decay time of the shortest flare F3 of V368 Cep was found to be 0.5 ks. In XI Boo, after the flare F6 an active level U was identified, where average flux was 1.8 times more than that of the Q state (see Fig. 1b), that was higher than the peak of the flare F5 indicating a very high activity level. Two similar highly active regions U1 and U2 were identified between the flares F13 and F14. The average fluxes during the regions U1 and U2 were 1.3 and 1.4 times more than that of the quiescent state. Presence of strong substructures in these active regions indicates superposition of a large number of flaring regions.

To investigate the behaviour of the flares detected in different energy bands, the light curves of the stars obtained with the MOS and PN are divided into three energy bands namely soft (0.3–0.8 keV), medium (0.8–1.6 keV) and hard (1.6–10 keV). The boundaries of the selected energy bands are chosen as the line-free regions of the low-resolution PN spectra. The hardness ratio HR1 and HR2 are defined by the ratio of medium to soft band, and hard to medium band count rate, respectively. The soft, medium, hard band intensity curves, and the hardness ratio curves HR1 and HR2 as a function of time are shown in the subpanels running from top to bottom in left (MOS) and right (PN) of Fig. 2(a) for the star V368 Cep. Similar plots of intensity and hardness ratios observed from the stars XI Boo, IM Vir, V471 Tau, CC Eri and EP Eri are shown in the Figs 2(b)–(f), respectively. The light curves in individual band also show significant variability in all sources. We have determined the e-folding decay time of observed flares in the three bands by fitting equation (1). The decay times, rise times, count rates at flare peaks and quiescent state count rates at soft, medium and hard band for PN data are given in the Table 5. For most of the flares, e-folding decay time in the soft band was found to be more than the decay

[1] http://heasarc.gsfc.nasa.gov/Tools/w3pimms.html

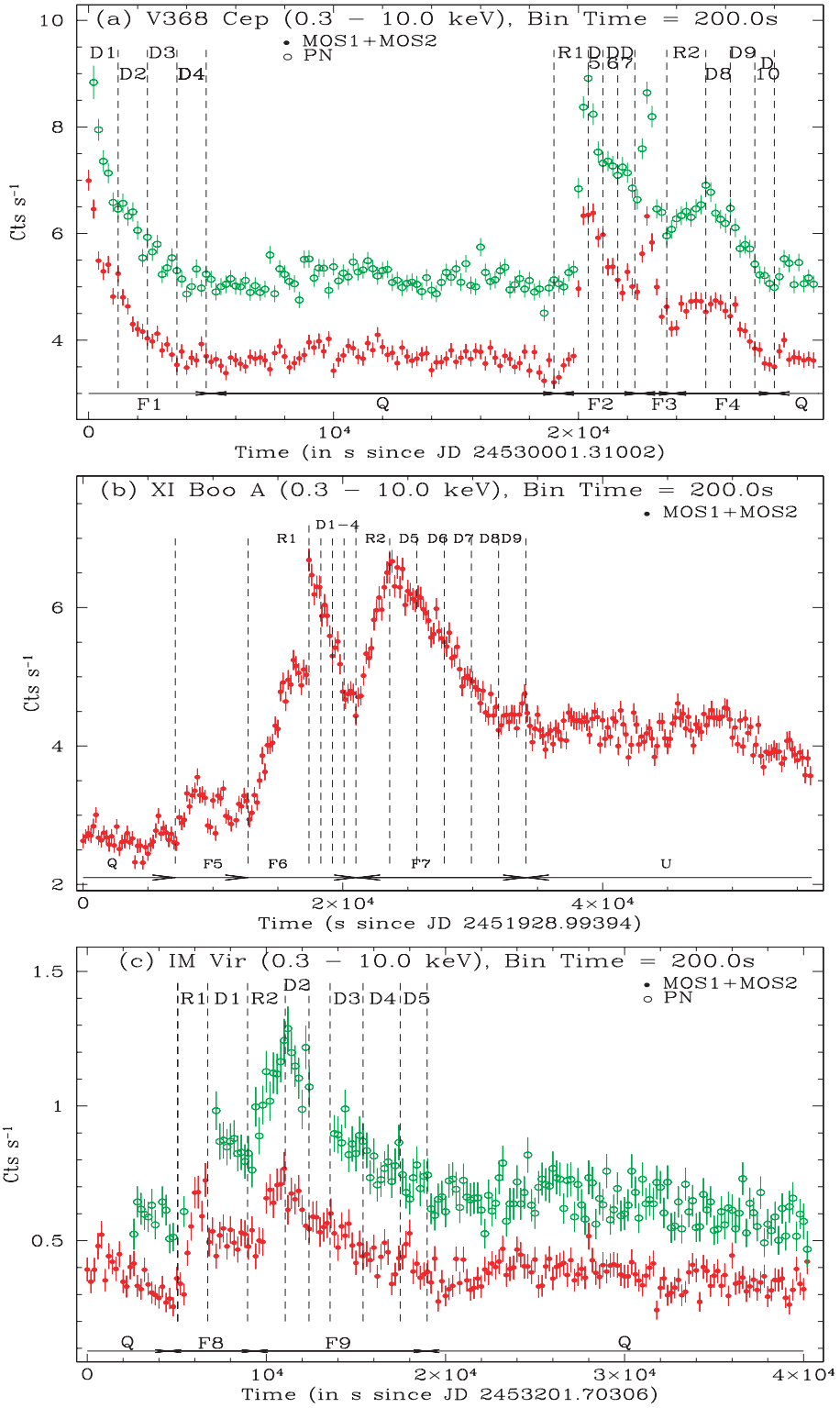

Figure 1. MOS and PN light curves of six G–K dwarfs.

time in the medium and the hard band. However, for the flare F3 of V368 Cep and F7 of XI Boo, it appears that decay time in the medium band was more than in the soft band. For the flares F6, F7 and F9 the decay time in the soft band was found to be more than 3.0 ks than that of the hard band. However, for other flare events the decay time in the soft band was $\lesssim$2 ks than that in the hard band. Two smaller flare like structures were seen just after the peak of flare F13 of CC Eri in the hard band but were not observed in the soft and medium band light curves (see Fig. 2e). The rise time for all flares in all band was found to be well within 1σ level (Table 5).

The flare peak to the quiescent state flux ratio in the hard band was found in between 2 and 16, which is more than that of the

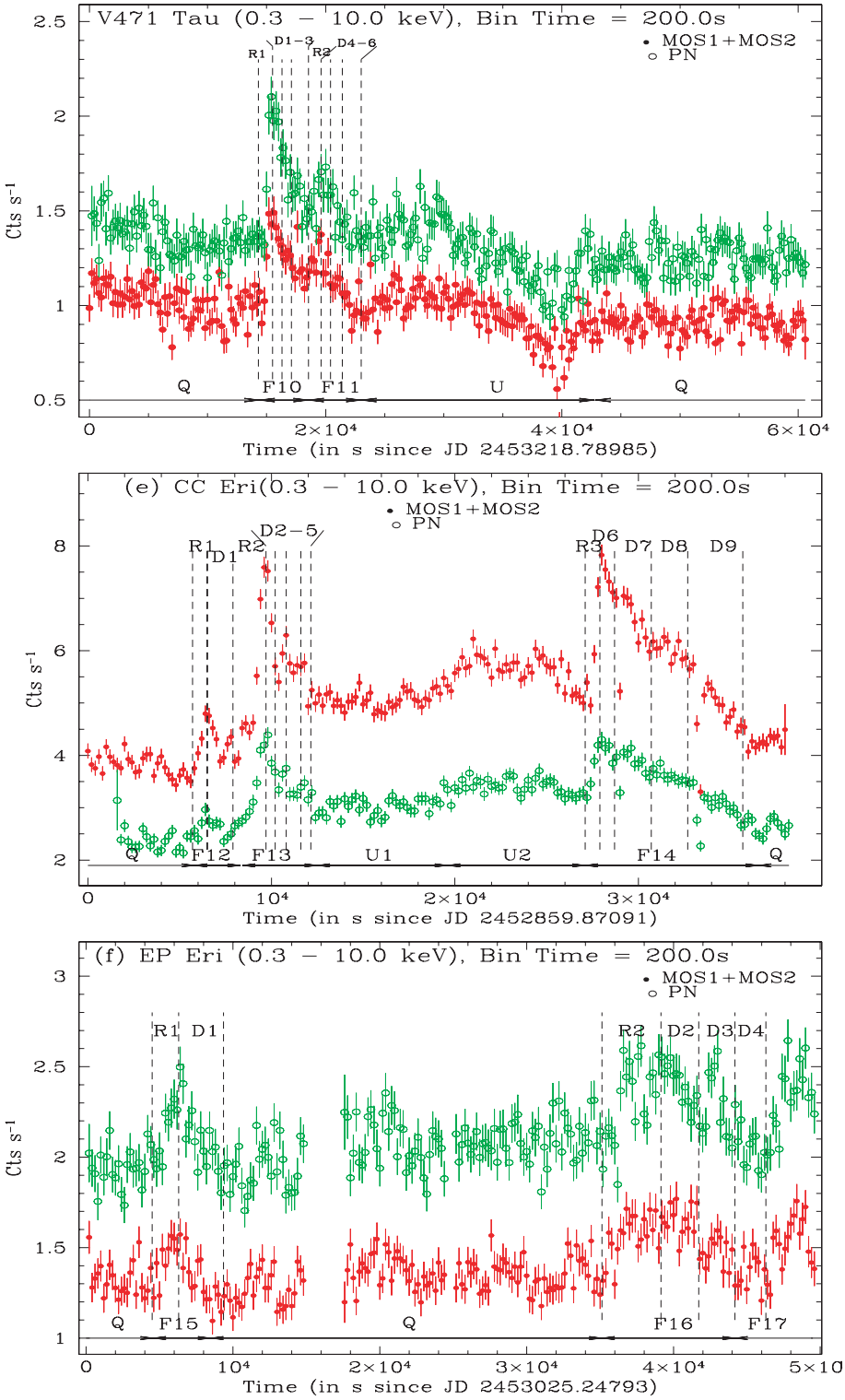

Figure 1 – *continued*

similar ratios in the medium and the soft band (see also Table 5) for all flares. In terms of the peak flux, the flares F6 and F7 of XI Boo, and F13 and F14 of CC Eri were stronger in the medium band than in the soft and the hard band. The variation in the hardness ratio is indicative of changes in coronal temperature. An X-ray flare is well defined by a rise in the temperature and subsequent decay. For the flares F6, F7, F9, F12, F13 and F14, both HR1 and HR2 varied in the similar fashion to their light curves (see Fig. 2). This implies that an increase in the temperature at flare peak and subsequent cooling. The structures observed during the decay phase of the flares F2 of V368 Cep and F13 of CC Eri in the hard band were also observed in the HR2 curve. This could probably be due to emergence of flares during the decay phase of these flares, which were comparatively stronger in the hard band. During the flares F2,

Table 3. Time interval of 17 flares observed in six G–K dwarfs.

Object	Flare	Time interval (ks after the observation start)	Duration (ks)	Peak flare flux[a] (10^{-11} erg s^{-1} cm^{-2})	Quiescent state flux[a] (10^{-11} erg s^{-1} cm^{-2})
V368 Cep	F1	...–4.0	4.0	2.28	1.30
	F2	19.2–22.5	3.3	2.39	...
	F3	22.5–23.9	1.4	2.36	...
	F4	23.9–27.8	3.9	1.90	...
XI Boo	F5	8.1–12.7	4.6	2.87	2.14
	F6	12.7–21.1	8.4	5.66	...
	F7	21.1–32.4	11.3	5.57	...
IM Vir	F8	4.5–9.3	4.8	0.20	0.13
	F9	9.3–18.9	9.6	0.25	...
V471 Tau	F10	14.4–18.5	4.1	0.39	0.24
	F11	18.5–23.0	4.5	0.31	...
CC Eri	F12	5.8–7.5	1.7	2.38	1.83
	F13	8.3–12.5	4.2	3.45	...
	F14	27.1–36.5	9.4	3.43	...
EP Eri	F15	4.5–8.5	4.0	0.62	0.48
	F16	35.1–44.2	8.9	0.65	...
	F17	47.4–...	...	0.66	...

[a]Count rates are converted into the flux using WebPIMMS (http://heasarc.gsfc.nasa.gov/Tools/w3pimms.html).

Table 4. Parameters obtained from fitting of equation (1) to the flare light curves obtained with MOS and PN detectors in the energy band of 0.3–10.0 keV.

Object name	FN	MOS				PN				L_X[a] (10^{29} erg s^{-1})	E_{tot} (10^{33} erg)
		A_0 (count s^{-1})	τ_d (s)	τ_r (s)	q (count s^{-1})	A_0 (count s^{-1})	τ_d (s)	τ_r (s)	q (count s^{-1})		
V368 Cep	F1	7.0 ± 0.2	1213 ± 74	...	3.6	9.0 ± 0.2	1226 ± 86	...	5.1	31.3	12.5
	F2	6.8 ± 0.1	1658 ± 141	315 ± 43		9.1 ± 0.3	2387 ± 341	347 ± 53		39.6	13.1
	F3	6.5 ± 0.2	451 ± 49	479 ± 44		8.7 ± 0.2	496 ± 36	515 ± 79		9.5	9.5
	F4	4.5 ± 0.3	1117 ± 110	649 ± 181		7.0 ± 0.2	1232 ± 133	681 ± 91		29.9	11.7
XI Boo	F5	3.42 ± 0.12	2829 ± 950	879 ± 213	2.66	...	...	...		0.5	0.23
	F6	6.9 ± 0.1	4393 ± 333	3169 ± 259		...	...	...		4.3	3.61
	F7	6.78 ± 0.06	9885 ± 362	3351 ± 244		...	...	...		5.7	6.44
IM Vir	F8	0.67 ± 0.04	1949 ± 578	205 ± 130	0.357	1.02 ± 0.05	2025 ± 603	311 ± 121	0.64	27.9	13.4
	F9	0.77 ± 0.02	3474 ± 680	1323 ± 277		1.27 ± 0.04	3450 ± 289	2041 ± 401		63.7	61.2
V471 Tau	F10	1.44 ± 0.04	2874 ± 605	595 ± 204	0.96	2.12 ± 0.05	2135 ± 286	580 ± 109	1.28	42.4	17.4
	F11	1.31 ± 0.03	1272 ± 301	864 ± 189		1.70 ± 0.02	1847 ± 519	827 ± 307		38.3	17.2
CC Eri	F12	4.9 ± 0.3	656 ± 152	256 ± 100	3.86	4.6 ± 0.2	781 ± 98	335 ± 52	2.35	2.0	0.34
	F13	6.9 ± 0.2	3027 ± 441	493 ± 50		6.4 ± 0.3	2844 ± 312	722 ± 61		6.7	2.82
	F14	7.9 ± 0.1	4800 ± 188	577 ± 91		7.4 ± 0.2	5992 ± 231	915 ± 51		6.7	6.26
EP Eri	F15	1.59 ± 0.04	939 ± 340	897 ± 439	1.20	2.48 ± 0.10	1094 ± 293	967 ± 201	1.90	1.4	0.56
	F16	1.72 ± 0.04	4476 ± 867	2800 ± 1103		2.54 ± 0.04	4052 ± 514	3200 ± 780		3.1	2.76
	F17	1.68 ± 0.03	...	820 ± 136		2.51 ± 0.03		1014 ± 597		0.8	

[a]L_X for each flare is integrated using the values given in Table 6 based on spectral fits.
Note. FN is flare name; A_0 is count rate at flare peak; τ_d is flare decay time; τ_r is flare rise time; q is quiescent state count rate; L_X is total X-ray luminosity during the flare and E_{tot} is total X-ray energy emitted during the flare.

F3 and F4 of V368 Cep, and F16 of EP Eri the HR1 did not show any variation but HR2 varied according to the flare intensity. However, HR1 and HR2 did not show any significant variation during the flares F1, F5, F8, F10, F11, F15 and F17. The PN data have more count rates than the MOS and have similar characteristics to that of MOS; therefore, for further analysis in this paper we use only the PN data.

4.2 Colour–colour diagrams

Plots of hardness ratio in the form of colour–colour (CC) diagram can reveal information about spectral variations and serve as a guide for a more detailed spectral analysis. For this purpose, the light curves and the hardness ratio curves of the flares were divided into different time segments covering their rising and decaying phases as shown in Fig. 1, where Ri ($i = 1, 2, \ldots$) represents the rising phase, Di ($i = 1, 2, \ldots$) represents the decay phase and Q represents the quiescent state. We determined the HR1 and HR2 from the PN data for each of these segments and plotted the values in Fig. 3. To understand the observed behaviour of HR1 and HR2 in terms of simple spectral models, we generated the soft (0.3–0.8 keV), medium (0.8–1.6 keV) and hard (1.6–10.0 keV) band count rate using the FAKEIT provision in the XSPEC, using the most recent canned response matrices downloaded from http://xmm.vilspa.esa.es/external/xmm_SW_cal/calib/epic_files.html and simple two-temperature plasma models. The

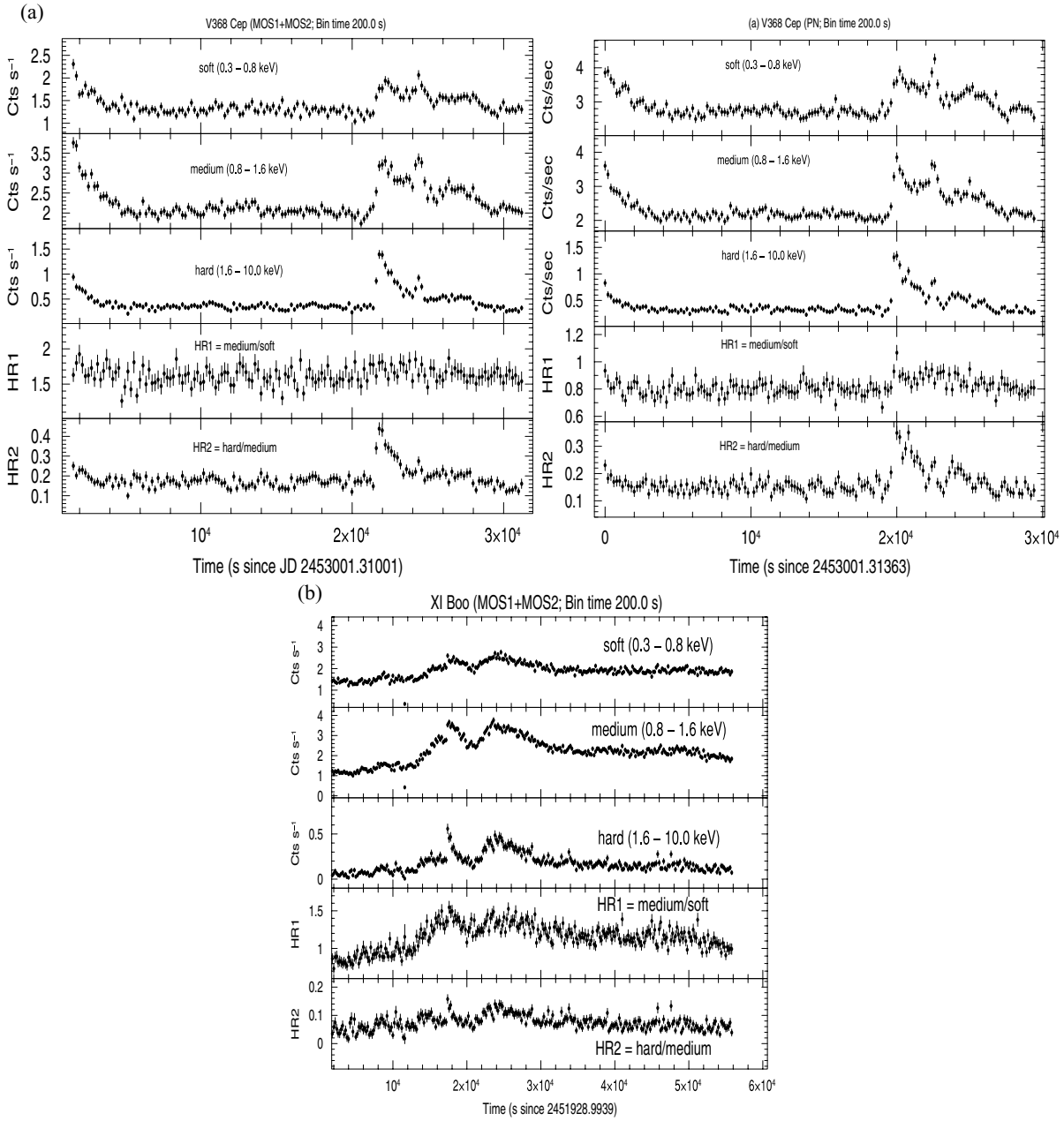

Figure 2. (a) MOS and PN light curves at three bands: soft (0.3–0.8 keV), medium (0.8–1.6 keV) and hard (1.6–10.0 keV), and hardness ratio HR1 and HR2 curve, where HR1 = medium/soft and HR2 = hard/medium of V368 Cep. (b) Similar to (a), but for XI Boo (only MOS). (c) Similar to (a), but for IM Vir. (d) Similar to (a), but for V471 Tau. (e) Similar to (a), but for CC Eri. (f) Similar to (a), but for EP Eri.

two-temperature APEC (Astrophysical Plasma Emission Code) models were mixed such that the emission measures (EMs) were in the ratio EM_2/EM_1 of 0.4, 0.6, 0.8, 1.0 and 1.2 (based on spectral results in Sections 4.3 and 4.4). The abundances (0.25) and hydrogen column density (10^{20} cm^{-2}) were kept fixed for each set of the EM_2/EM_1 (see Sections 4.3 and 4.4). Further by keeping kT_1 fixed at different values ranging from 0.2 to 1.2 keV in steps of 0.2 and varying kT_2 from 0.4 to 2.4 keV such that $kT_2 > kT_1$, we generated count rates in the soft, medium and hard bands. These predicted count rates were used to generate the hardness ratios. The families of curve thus generated are overplotted on the data points in Fig. 3 to understand the CC diagram. The kT_2 in Fig. 3 increases from bottom to top of each curve.

Fig. 3(a) shows the plot between HR1 and HR2 for a set of $EM_2/EM_1 = 1.0$ for the star V368 Cep. In the case of the flare F1, 'D1' intersects the generated CC curves for which kT_1 is 0.6 keV, however, 'D4' intersects the curve generated for $kT_1 = 0.2$ keV. A similar pattern is seen for the other flares F2 and F4 of the stars V368 Cep, where the top of the flare is located near the CC curve for a high-temperature component whereas the colours near the end of the flare intersect the CC curve corresponding to a lower temperature. The flare F2 shows a very high temperature during its rise phase 'R1' and the decay phase 'D5', as both are located between the CC curves of 1.0 and 1.2 keV. The decay phase D6 of the flare F2 is located near the 0.8 keV CC curve. The peak seen during the decay phase D6 of flare F2 (Fig 3a) can be explained by a rise in the

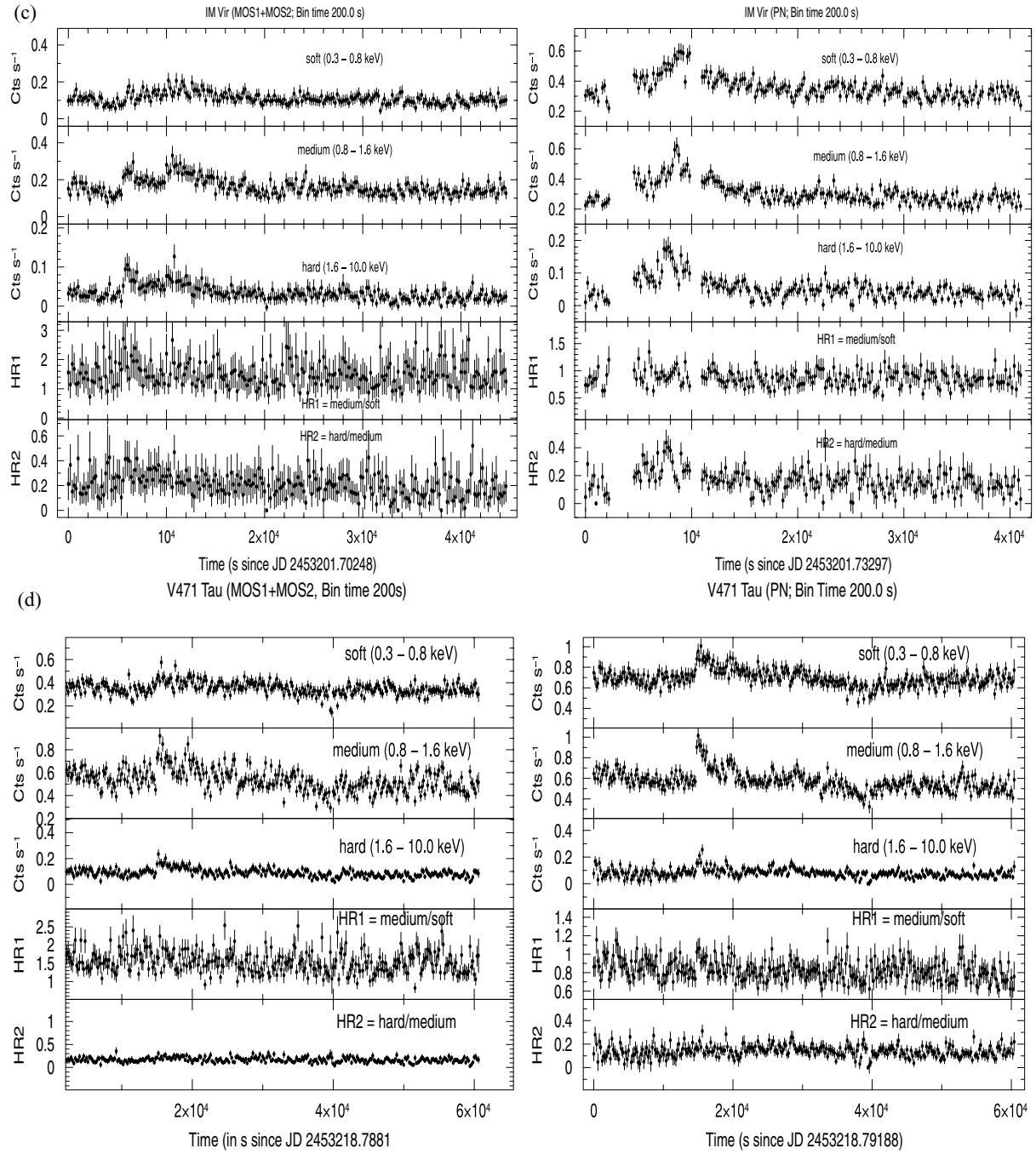

Figure 2 – *continued*

temperature of coronal plasma. It appears that the quiescent state 'Q' of the star V368 Cep has a cool temperature between 0.2 and 0.4 keV.

The peak of the largest flare 'F9' observed in the star IM Vir appears to have a temperature between 1.0 and 1.2 keV. As the flare decayed the temperature was also observed to decrease. A similar trend is seen during the flares observed in the stars XI Boo (Fig. 3b), V471 Tau (Fig. 3d), CC Eri (Fig. 3e) and EP Eri (Fig. 3f). The observed CC curves for the star IM Vir, V471 Tau and CC Eri were well matched with the generated family of CC curves for a set of $EM_1/EM_2 = 1.0$. However, the observed CC diagram of EP Eri were well matched with generated CC curves for a set of $EM_1/EM_2 =$ 0.4. It appears that high temperatures are needed during the flare peak, and the plasma temperatures decrease as flare decays. To further confirm and quantify the spectral changes during the flare, we have also performed a detailed spectral analysis of the flares and the quiescent states of the stars. The results of these analyses are presented below.

4.3 Quiescent state X-ray spectra

X-ray spectra for each star during the quiescent state were analysed using XSPEC, version 12.3 (Arnaud 1996). Data were cleaned of proton flares by removing the affected time periods for the stars IM Vir

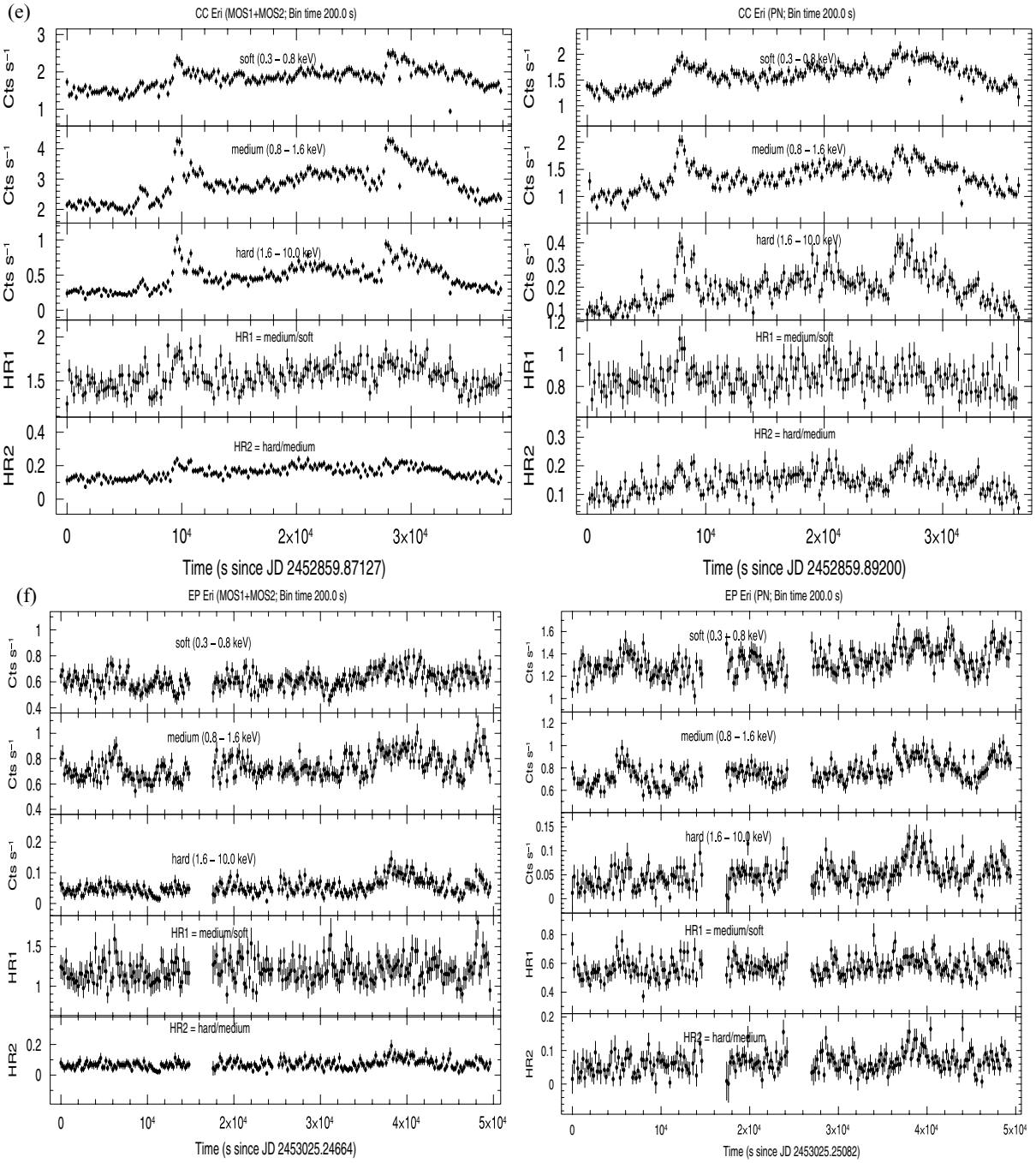

Figure 2 – *continued*

and EP Eri. Spectral analysis of EPIC data was performed in the energy band between 0.3 and 10.0 keV for the star V368 Cep, XI Boo, V471 Tau and CC Eri, while for the stars IM Vir and EP Eri spectral analysis was performed between 0.3 and 5.1 keV. Individual spectra were binned so as to have a minimum of 20 counts per energy bin. The EPIC spectra of the stars were fitted with a single (1T) and two (2T) temperature collisional plasma model known as APEC (Smith et al. 2001), with variable elemental abundances. Abundances for all the elements in the APEC were varied together. The interstellar hydrogen column density ($N_{\rm H}$) was left free to vary. For all the stars, no 1T or 2T plasma models with solar photospheric (Anders & Grevesse 1989) abundances could fit the data, as unacceptably large values of χ^2_ν were obtained. Acceptable APEC 2T fits were achieved only when the abundances were allowed to depart from the solar values. The best-fitting 2T plasma models with subsolar abundances along with the significance of the residuals in terms of $\Delta\chi^2$ are shown in Figs 4(a)–(f) for all the stars. Table 6 summarizes the best-fitting values obtained for the various parameters along with the minimum $\chi^2_\nu = \chi^2/\nu$ (where ν is degrees of freedom) and the 90 per cent confidence error bars estimated from the minimum $\chi^2 + 2.71$. The derived values $N_{\rm H}$ from the spectral analysis were found to be lower than that of the total galactic H I column density

Table 5. Parameters obtained from the fitting of flare light curves observed with PN detector in the soft, medium and hard bands.

Object name	FN	Soft (0.3–0.8 keV)				Medium (0.8–1.6 keV)				Hard (1.6–10.0 keV)			
		τ_d (s)	τ_r (s)	A_0 (count s^{-1})	q (count s^{-1})	τ_d (s)	τ_r (s)	A_0 (count s^{-1})	q (count s^{-1})	τ_d (s)	τ_r (s)	A_0 (count s^{-1})	q (count s^{-1})
V368 Cep	F1	1485 ± 171	...	3.96 ± 0.09	2.69	1105 ± 110	...	3.54 ± 0.09	2.15	840 ± 97	...	0.74 ± 0.03	0.31
	F2	2749 ± 747	374 ± 79	3.90 ± 0.07	...	1949 ± 318	249 ± 43	3.86 ± 0.07	...	1546 ± 212	186 ± 37	1.35 ± 0.05	...
	F3	318 ± 47	545 ± 90	4.21 ± 0.10	...	610 ± 113	707 ± 184	3.45 ± 0.10	...	324 ± 45	283 ± 56	0.81 ± 0.07	...
	F4	1258 ± 264	545 ± 90	3.46 ± 0.10	...	1184 ± 156	792 ± 201	3.02 ± 0.07	...	1130 ± 330	709 ± 224	0.52 ± 0.04	...
XI Boo	F6	5552 ± 748	2821 ± 235	2.62 ± 0.04	1.40	4665 ± 340	3429 ± 291	3.74 ± 0.07	1.22	2120 ± 191		0.47 ± 0.02	0.05
	F7	10155 ± 786	4120 ± 643	2.66 ± 0.03	...	10599 ± 543	3320 ± 296	3.86 ± 0.04	...	6772 ± 492	2683 ± 556	0.46 ± 0.01	...
IM Vir	F9	3810 ± 455	1194 ± 296	0.56 ± 0.02	0.32	3226 ± 427	848 ± 112	0.56 ± 0.02	0.27	790 ± 130	350 ± 171	0.21 ± 0.01	0.06
V471 Tau	F10	2945 ± 530	851 ± 146	0.98 ± 0.03	0.65	2465 ± 454	676 ± 179	0.98 ± 0.03	0.53	1409 ± 549	806 ± 251	0.18 ± 0.02	0.07
	F11	1962 ± 267	1203 ± 272	0.87 ± 0.03	...	1254 ± 258	1149 ± 209	0.77 ± 0.03	...	278 ± 121	247 ± 106	0.16 ± 0.02	...
CC Eri	F12	591 ± 149	383 ± 99	1.62 ± 0.08	1.27	641 ± 90	503 ± 151	2.22 ± 0.08	1.27	452 ± 138	460 ± 123	0.33 ± 0.04	0.07
	F13	3182 ± 501	800 ± 115	2.99 ± 0.09	...	2429 ± 232	712 ± 92	4.23 ± 0.05	...	2245 ± 551	692 ± 153	1.03 ± 0.10	...
	F14	6445 ± 334	1552 ± 138	3.40 ± 0.06	...	5765 ± 360	1262 ± 194	3.87 ± 0.10	...	3934 ± 252	513 ± 93	1.14 ± 0.05	...
EP Eri	F15	1223 ± 256	609 ± 194	1.51 ± 0.03	1.21	715 ± 255	601 ± 201	0.91 ± 0.07	0.68	...	...	...	...

Note. FN is flare name; A_0 is count at flare peak; τ_d is flare decay time; τ_r is flare rise time; q is the quiescent state count rates.

(Dickey & Lockman 1990) towards the direction of that star. The cool and hot temperatures at the quiescent state of these stars were found in the range of 0.2–0.5 and 0.6–1.0 keV, respectively. The corresponding EM_2/EM_1 during the quiescent state of each star was found in the range of 0.8–1.2, except for the star EP Eri where it was found to be ∼0.4.

4.4 Spectral evolution of X-ray flares

In order to trace the spectral changes during the flares, we have analysed the spectra of the different time intervals shown in Fig. 1. To study the flare emission only, we have performed 1T spectral fits of the data, with the quiescent emission taken into account by including its best-fitting 2T model as a frozen background contribution. This is equivalent to consider the flare emission subtracted of the quiescent level, allows us to derive one 'effective' temperature and one EM of the flaring plasma. The abundances were kept fix to that of the quiescent emission. The best-fitting spectral parameters for each flare segments are listed in Table 7. Figs 5–10 show the temporal evolution of the temperature and corresponding EM of the flares detected in the targeted stars, where '0' time corresponds to the flare peak time.

4.4.1 V368 Cep

Spectral data of flares F1, F2 and F4 were binned into four segments. However, for the flare F3 data could be collected over only one segment. Both the temperature and the corresponding EM were found to decrease from the flare peak to the quiescent state (see also Table 7). As shown in Fig. 5(a), the highest temperature for the flare F1 was 14 MK and decreased along the decay path to 6.8 MK. A similar trend was also found in the EM, where it increased by a factor of 7 (see Fig. 5b). The temperature and EM for the flare F2 were peaked simultaneously during the decay phase D5. However, for the flare F4 both parameters were peaked during the rise phase R2. The maximum luminosity was found during the flares F2 and peaked at 1.18×10^{30} erg s^{-1}, which is ∼1.7 times more than that of the quiescent state.

4.4.2 XI Boo

To see the flare evolution, flare F6 and F7 have binned into five and six intervals, respectively. For the flare segments R2, D5, D6, D7 and D8, the 1T APEC fit gave high value of χ^2_ν (=1.5 for R2, 1.75 for D5, 1.61 for D6, 1.55 for D7 and 1.34 for D8). The spectral fit to the data for these time segments improves the χ^2 by using the 2T plasma model (see Table 7). The temperature and the corresponding EM of the cool component for these time segments were found to be constant at 0.6 ± 0.1 keV and $4.0 \pm 1.0 \times 10^{51}$ cm^{-3}, respectively. The spectral parameters for hot component of the best-fitting 2T plasma model are reported in Table 7. The evolution of the temperature of hot component and the corresponding EM are shown in Figs 6(a) and (b), respectively. For the flares F6 and F7, both the temperature and corresponding EM were reached to the maximum value during the decay phase. As mentioned in Tables 6 and 7, during the flares F6 and F7, XI Boo was ∼two times more X-ray luminous than that of the quiescent state.

4.4.3 IM vir

The spectral data of the flares F8 and F9 were binned in two and four different time segments, respectively (see Fig. 1c), and spectra of each segment were fitted with 1T APEC model. The plots of

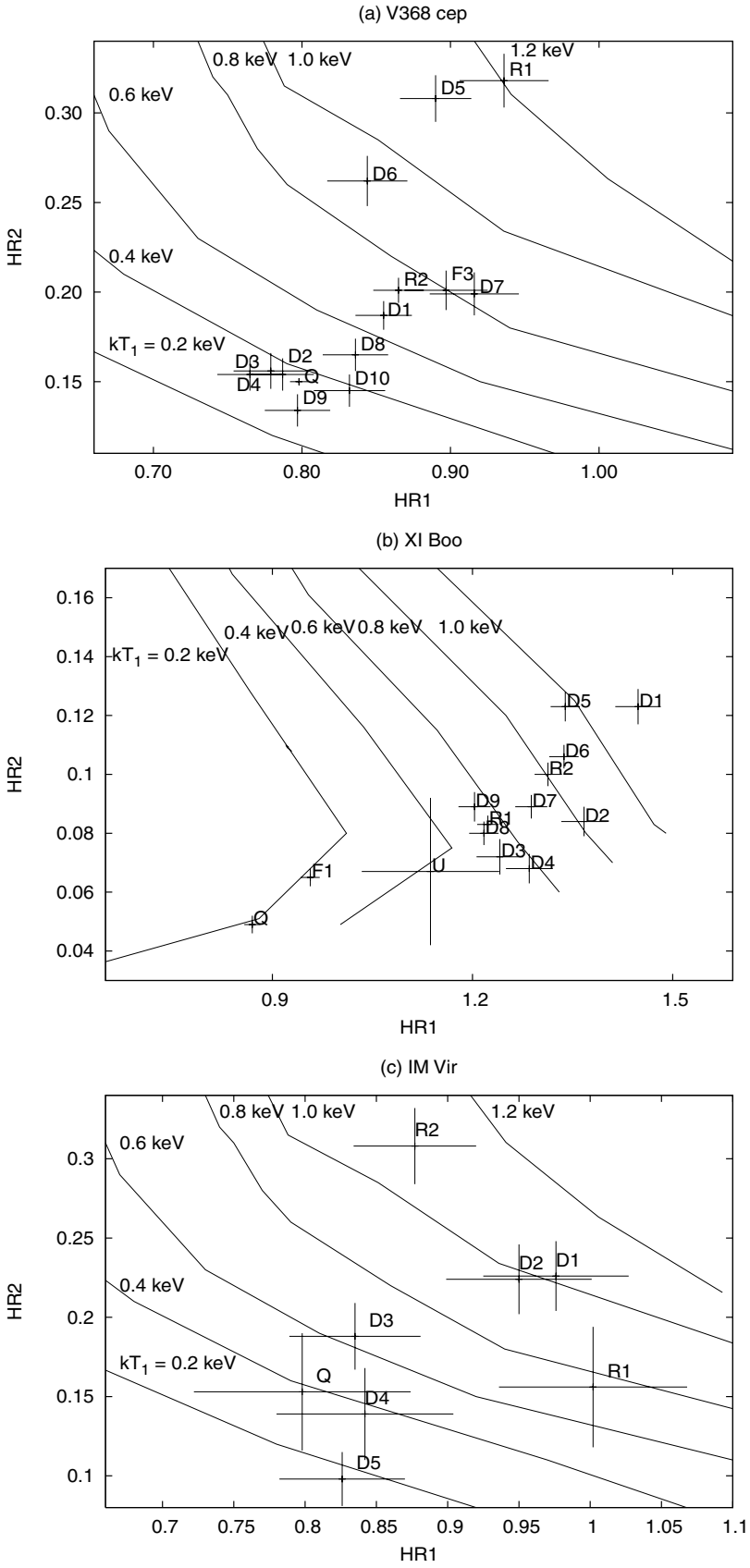

Figure 3. CC diagram (HR1 versus HR2) for the various time segments (Q: quiescent state; Ri ($i = 1, 2, \ldots$): rise phase; Di ($i = 1, 2, \ldots$): decay phase) observed for each source. The curves overplotted on the data are for model simulation where two-temperature plasma is assumed to predict the colours (see Section 4.2 for details).

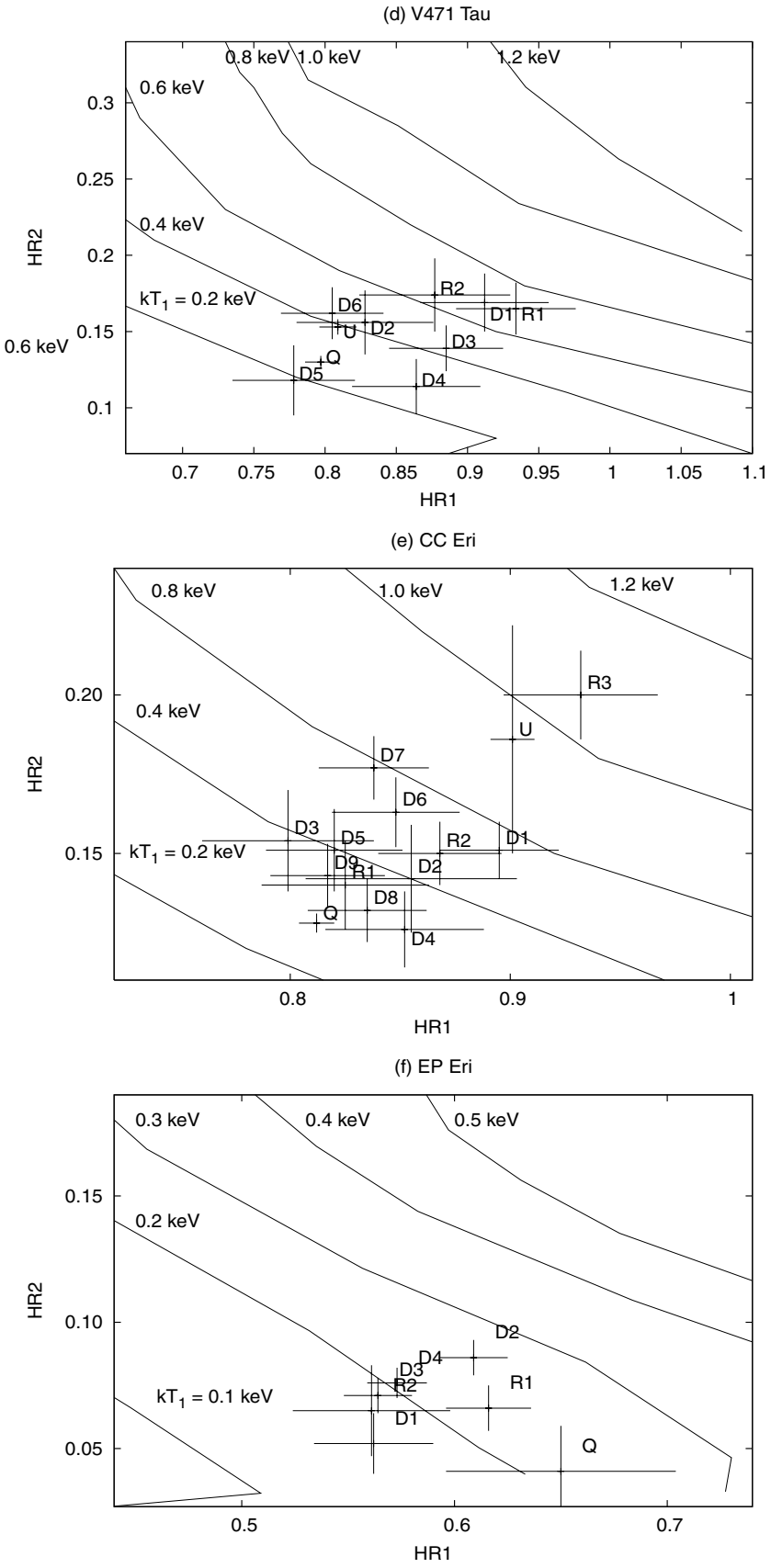

Figure 3 – *continued*

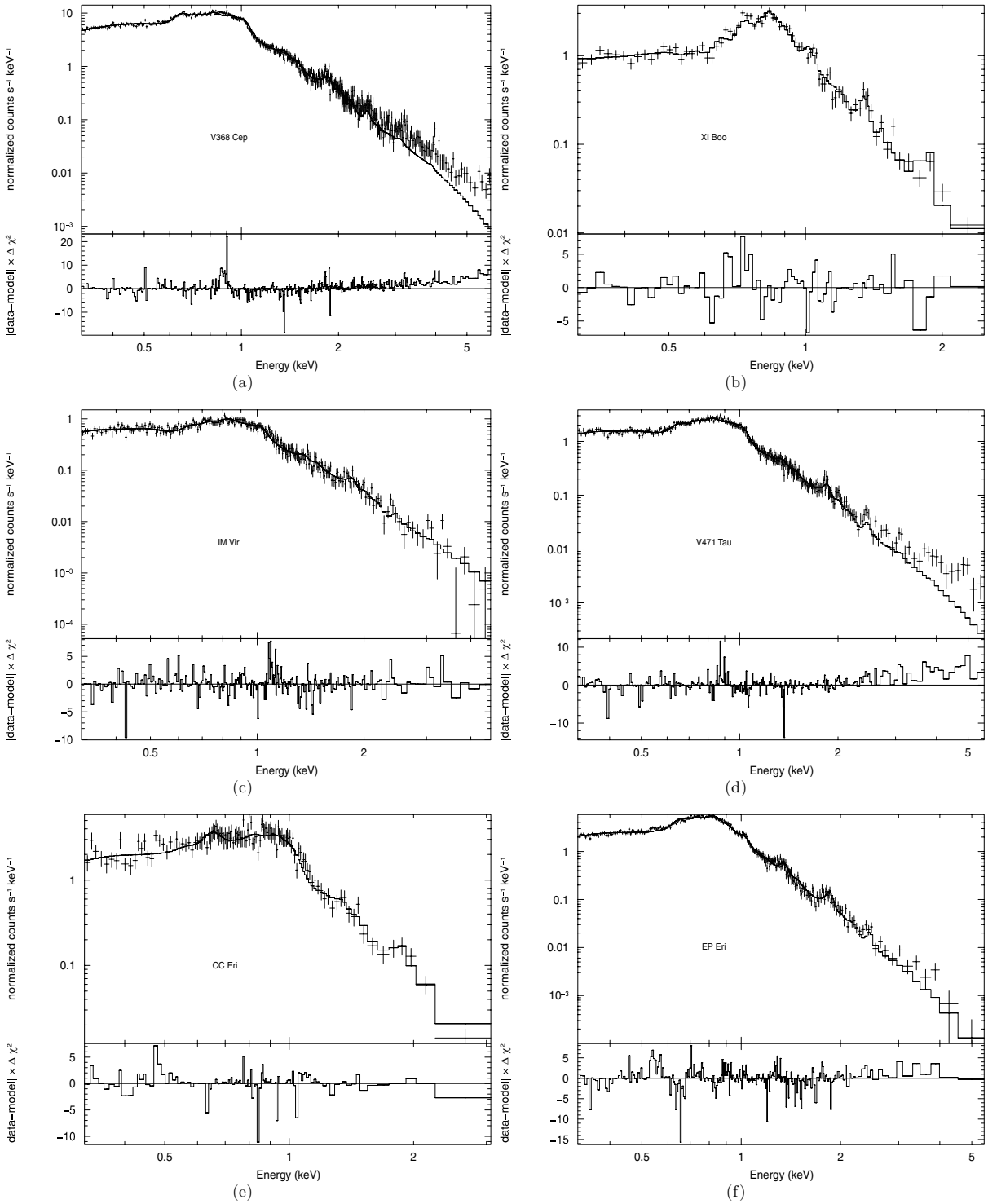

Figure 4. Quiescent state spectra of PN data with APEC 2T model in upper subpanels of each graph. χ^2 contributions are given in the lower subpanel of the each graph.

temperature and the corresponding EM are shown in Figs 7(a) and (b), respectively. For the flare F9, the maximum fit temperature was reached during the rising phase R2, somewhat earlier than the maximum of its EM. The EM was increased by a factor of 4 during the flare F9. The luminosity at the peak of flare F9 was found to be ∼two times more than that of the quiescent state.

4.4.4 V471 Tau

Two flares detected in the star V471 Tau were examined by analysing four different time intervals during the flares. Figs 8(a) and (b) show the plot of temperature and the corresponding EM during the flares F10 and F11. For the flare F10 the temperature reached its maximum value of 17.8 MK and decreased along the decay phase (see Table 7).

Table 6. Spectral parameters derived for the quiescent emission of each program star from the analysis of PN spectra (MOS spectra for XI Boo) accumulated during the time interval 'Q' as shown in Fig. 1, using APEC 2T model.

Object	$N_{\rm H}$	Z	kT_1	$\rm EM_1$	kT_2	$\rm EM_2$	$L_{\rm X}$	χ^2_ν (DOF)
V368 Cep	$1.9^{+0.4}_{-0.5}$	$0.14^{+0.01}_{-0.01}$	$0.35^{+0.01}_{-0.01}$	$7.4^{+0.5}_{-0.6}$	$0.90^{+0.01}_{-0.01}$	$5.9^{+0.2}_{-0.3}$	6.8	1.71 (429)
XI Boo	<0.95	<0.23	$0.20^{+0.08}_{-0.04}$	$1.51^{+0.70}_{-0.51}$	$0.57^{+0.01}_{-0.01}$	$1.2^{+0.1}_{-0.1}$	0.51	1.68 (72)
IM Vir	$2.8^{+0.9}_{-1.0}$	$0.12^{+0.02}_{-0.02}$	$0.49^{+0.05}_{-0.04}$	$7.4^{+1.2}_{-1.1}$	$0.97^{+0.05}_{-0.04}$	$8.3^{+1.0}_{-2.3}$	8.3	1.13 (280)
V471 Tau	$2.4^{+0.6}_{-0.6}$	$0.16^{+0.02}_{-0.01}$	$0.41^{+0.02}_{-0.02}$	$6.2^{+0.7}_{-0.6}$	$0.90^{+0.02}_{-0.02}$	$6.5^{+0.4}_{-0.4}$	7.5	1.16 (341)
CC Eri	$1.3^{+0.8}_{-0.7}$	$0.18^{+0.02}_{-0.02}$	$0.31^{+0.01}_{-0.01}$	$0.6^{+0.2}_{-0.1}$	$0.83^{+0.07}_{-0.07}$	$0.5^{+0.2}_{-0.1}$	0.9	1.05 (302)
EP Eri	<0.4	$0.21^{+0.01}_{-0.01}$	$0.36^{+0.01}_{-0.01}$	$0.8^{+0.1}_{-0.2}$	$0.69^{+0.02}_{-0.03}$	$0.3^{+0.2}_{-0.1}$	0.7	1.44 (291)

Note. $N_{\rm H}$ is in 10^{20} cm^{-2} temperatures (kT) are in keV; EM is in 10^{52} cm^{-3} and X-ray luminosity ($L_{\rm X}$) is in 10^{29} erg s^{-1}. χ^2_ν is the minimum reduced χ^2 and DOF stands for degrees of freedom.

The corresponding EM was also peaked during the decay phase of the flare F10 (see Fig. 8b and Table 7). For the flare F11, both the temperature and the EM follow similar trend to the flare light curve. The X-ray luminosity was increased by a factor of $\sim$1.6 for the flare F10 and $\sim$1.4 for the flare F11.

4.4.5 CC Eri

The evolution of temperature and the corresponding EM for three flares F12, F13 and F14 are shown in Figs 9(a) and (b), respectively. Small variations were found in the temperature and the EM during the flares F13 and F14. Both the temperatures and the corresponding EMs were found to decrease during the decay phase for all flares (see also Table 7). The temperature and the corresponding EM for all the flares were peaked during the decay phase. However, it appears that temperature is peaked before the EM for the flare F13. The peak luminosity during flares F13 and F14 was found to be 6.0×10^{28} erg s^{-1} more than that of the quiescent state.

4.4.6 EP Eri

Spectra of different time segments of the flares are fitted with 1T plasma models. Figs 10(a) and (b) show the evolution of temperature and the corresponding EM for the flares F15 and F16. For the flare F16, both the temperature and the corresponding EM were peaked during the rise phase R2, remained constant up to the decay phase D2 and then decreased along the flare decay without any appreciable changes in the luminosity. The luminosity during both flares was found to be similar to that of the quiescent state (see Tables 6 and 7).

4.5 Loop modelling of the X-ray flares

Flares cannot be resolved spatially on a star. However, by an analogy with solar flares and using flare loop models, it is possible to infer the physical size and morphology of the loop structures involved in a stellar flare. The most widely used but approximate methods for analysing stellar flares are (i) two-ribbon flare method (Kopp & Poletto 1984), (ii) quasi-static cooling method (van den Oord & Mewe 1989), (iii) pure radiation cooling method (Pallavicini et al. 1990), (iv) rise and decay time method (Hawley et al. 1995) and (v) hydrodynamic method (Reale et al. 1997). The two-ribbon flare model assumes that the flare decay is entirely driven by heating released by magnetic reconnection of higher and higher loops and neglects completely the effect of plasma cooling. The other four methods are instead based on the cooling of plasma confined in a single flaring loop. In the hypothesis of flares occurring inside closed coronal structures, the decay time of the X-ray emission roughly scales as the plasma cooling time. In turn, the cooling time-scales with the length of the structure which confines the plasma: the longer the decay, the larger is the structure (e.g. Haisch et al. 1983). A loop thermodynamic decay time has been derived (van den Oord & Mewe 1989; Serio et al. 1991) as

$$\tau_{\rm th} = \frac{120 L_9}{\sqrt{T_7}}, \tag{2}$$

where L_9 and T_7 are the loop half-length and the maximum temperature ($T_{\rm max}$) of the flaring plasma, in units of 10^9 cm and 10^7 K, respectively. The time-scale above is derived under the hypothesis of impulsive heat released at the beginning of a flare.

The hydrodynamic model includes both plasma cooling and the effect of heating during flare decay. Reale et al. (1997) presented a method to infer the geometrical size and other relevant physical parameters of the flaring loops, based on the decay time and on evolution of temperature and the EM during the flare decay. The empirical formula for the estimation of the unresolved flaring loop length has been derived as

$$L_9 = \frac{\tau_{\rm d}\sqrt{T_7}}{120 f(\zeta)} \qquad f(\zeta) \geqslant 1, \tag{3}$$

where $\tau_{\rm d}$ is the decay time of the light curve, and $f(\zeta)$ is a non-dimensional correction factor larger than 1. ζ is the slope of the decay path in the density–temperature diagram (Sylwester et al. 1993) and is maximum ($\sim$2) if heating is negligible and minimum ($\sim$0.5) if heating dominates the decay. The correction factor $f(\zeta)$ and loop maximum temperature are calibrated for the *XMM–Newton* EPIC spectral response and are given as (Reale 2007)

$$f(\zeta) = \frac{0.51}{\zeta - 0.35} + 1.36 \qquad (\text{for } 0.35 < \zeta \leqslant 1.6), \tag{4}$$

$$T_{\rm max} = 0.13\, T_{\rm obs}^{1.16}. \tag{5}$$

Other physical properties of the flaring plasma can be inferred from the analysis of flare data. The analysis of X-ray spectra provides values of the temperature and EM. From the EM and the plasma density ($n_{\rm e}$), the volume of the flaring loop is estimated as (Reale 2002)

$$V = \frac{\rm EM}{n_{\rm e}^2}, \tag{6}$$

where V is the loop volume. It has been shown that in the equilibrium condition the loop scaling laws hold, linking maximum pressure,

Table 7. Spectral parameters for each temporal segment of the flare in the targeted stars. The temporal segments of the flare are marked by vertical lines in Fig. 1.

Object	LS	FS	kT	EM	L_X	χ^2_ν (DOF)
V368 Cep	F1	D1	$1.20^{+0.11}_{-0.10}$	$3.7^{+0.3}_{-0.3}$	9.4	0.97 (213)
		D2	$1.01^{+0.10}_{-0.04}$	$1.9^{+0.3}_{-0.3}$	8.0	1.11 (197)
		D3	$0.74^{+0.23}_{-0.11}$	$0.9^{+0.3}_{-0.3}$	7.2	0.94 (186)
		D4	$0.58^{+0.04}_{-0.15}$	$0.5^{+0.4}_{-0.2}$	6.7	0.82 (170)
	F2	R1	$2.40^{+0.35}_{-0.15}$	$3.0^{+0.4}_{-0.4}$	9.7	1.19 (157)
		D5	$2.61^{+0.33}_{-0.29}$	$4.7^{+0.1}_{-0.2}$	11.8	1.14 (220)
		D6	$2.46^{+0.28}_{-0.24}$	$3.5^{+0.3}_{-0.2}$	9.5	1.02 (163)
		D7	$1.86^{+0.26}_{-0.43}$	$3.4^{+0.2}_{-0.2}$	8.8	1.12 (163)
	F3	...	$0.98^{+0.07}_{-0.07}$	$4.6^{+0.6}_{-0.5}$	9.5	1.18 (234)
	F4	R2	$1.79^{+0.16}_{-0.23}$	$2.6^{+0.3}_{-0.3}$	8.2	1.06 (255)
		D8	$1.22^{+0.09}_{-0.07}$	$2.5^{+0.3}_{-0.3}$	8.2	0.88 (183)
		D9	$0.71^{+0.18}_{-0.07}$	$1.6^{+0.3}_{-0.3}$	7.1	1.04 (174)
		D10	$0.57^{+0.19}_{-0.12}$	$1.0^{+0.3}_{-0.3}$	6.4	0.96 (220)
XI Boo	F5	...	$0.81^{+0.21}_{-0.08}$	$0.10^{+0.02}_{-0.02}$	0.54	1.37 (89)
	F6	R1	$0.94^{+0.04}_{-0.04}$	$0.34^{+0.02}_{-0.02}$	0.74	1.17 (103)
		D1	$0.93^{+0.04}_{-0.04}$	$0.68^{+0.04}_{-0.04}$	1.02	0.97 (72)
		D2	$0.80^{+0.04}_{-0.04}$	$0.57^{+0.04}_{-0.04}$	0.93	0.90 (65)
		D3	$0.71^{+0.04}_{-0.05}$	$0.45^{+0.04}_{-0.04}$	0.83	0.87 (61)
		D4	$0.78^{+0.05}_{-0.05}$	$0.39^{+0.03}_{-0.03}$	0.78	1.21 (60)
	F7	R2[a]	$1.08^{+0.06}_{-0.12}$	$0.28^{+0.12}_{-0.06}$	0.93	1.27 (93)
		D5[a]	$1.15^{+0.14}_{-0.15}$	$0.42^{+0.15}_{-0.09}$	1.11	1.20 (85)
		D6[a]	$1.21^{+0.15}_{-0.11}$	$0.43^{+0.08}_{-0.10}$	1.07	0.93 (82)
		D7[a]	$1.04^{+0.18}_{-0.08}$	$0.33^{+0.10}_{-0.09}$	0.99	0.95 (81)
		D8[a]	$0.95^{+0.06}_{-0.05}$	$0.34^{+0.03}_{-0.06}$	0.88	1.09 (78)
		D9	$0.77^{+0.05}_{-0.03}$	$0.29^{+0.07}_{-0.03}$	0.73	1.07 (73)
IM Vir	F8	R1	<5.16	$7.8^{+2.4}_{-1.1}$	14.6	1.10 (60)
		D1	$3.23^{+1.56}_{-0.91}$	$5.0^{+1.2}_{-0.6}$	13.3	1.23 (88)
	F9	R2	$2.04^{+0.35}_{-0.14}$	$8.6^{+0.9}_{-1.0}$	15.9	1.08 (103)
		D2	$1.23^{+0.10}_{-0.14}$	$11.2^{+1.5}_{-1.5}$	15.8	0.86 (36)
		D3	$0.89^{+0.15}_{-0.10}$	$5.8^{+0.8}_{-0.8}$	11.8	1.22 (77)
		D4	$1.02^{+0.27}_{-0.13}$	$3.0^{+0.7}_{-0.7}$	10.3	1.12 (81)
		D5	$0.72^{+0.18}_{-0.12}$	$2.8^{+0.7}_{-0.7}$	9.90	0.79 (31)
V471 Tau	F10	R1	$1.23^{+0.12}_{-0.12}$	$4.4^{+0.8}_{-0.8}$	10.6	0.85 (49)
		D1	$1.29^{+0.14}_{-0.17}$	$5.6^{+0.7}_{-0.7}$	12.3	1.18 (74)
		D2	$1.24^{+0.09}_{-0.14}$	$3.5^{+0.6}_{-0.6}$	10.3	1.03 (64)
		D3	$1.08^{+0.07}_{-0.12}$	$2.3^{+0.5}_{-0.5}$	9.2	0.80 (80)
	F11	R2	$1.86^{+2.13}_{-0.90}$	$2.6^{+0.9}_{-0.9}$	10.8	1.14 (43)
		D4	$0.91^{+0.21}_{-0.15}$	$3.2^{+0.7}_{-0.7}$	9.7	0.89 (50)
		D5	<2.79	$1.3^{+0.6}_{-0.6}$	9.5	1.35 (56)
		D6	<1.48	$0.7^{+0.5}_{-0.3}$	8.3	0.79 (72)
CC Eri	F12	R1	> 1.03	$0.12^{+0.06}_{-0.05}$	1.0	0.85 (74)
		D1	$2.37^{+1.45}_{-0.77}$	$0.14^{+0.05}_{-0.04}$	1.0	1.24 (135)
	F13	R2	$1.23^{+0.12}_{-0.12}$	$0.52^{+0.05}_{-0.05}$	1.3	1.14 (129)
		D2	$1.17^{+0.11}_{-0.18}$	$0.77^{+0.07}_{-0.07}$	1.5	1.24 (82)
		D3	$1.23^{+0.25}_{-0.13}$	$0.52^{+0.06}_{-0.06}$	1.3	1.26 (86)
		D4	$1.00^{+0.19}_{-0.10}$	$0.45^{+0.05}_{-0.05}$	1.3	0.87 (101)
		D5	$0.97^{+0.15}_{-0.07}$	$0.43^{+0.05}_{-0.05}$	1.2	0.91 (126)
	F14	R3	$1.23^{+0.12}_{-0.12}$	$0.52^{+0.05}_{-0.05}$	1.3	1.14 (129)
		D6	$1.28^{+0.35}_{-0.10}$	$0.80^{+0.06}_{-0.06}$	1.5	1.32 (120)
		D7	$1.21^{+0.07}_{-0.07}$	$0.70^{+0.04}_{-0.04}$	1.4	1.20 (218)
		D8	$1.02^{+0.19}_{-0.06}$	$0.59^{+0.04}_{-0.04}$	1.3	1.27 (209)
		D9	$0.98^{+0.09}_{-0.09}$	$0.31^{+0.04}_{-0.04}$	1.2	1.17 (217)
EP Eri	F15	R1	$0.68^{+0.21}_{-0.20}$	$0.13^{+0.06}_{-0.05}$	0.7	1.24 (74)
		D1	$0.57^{+0.16}_{-0.20}$	$0.17^{+0.09}_{-0.05}$	0.7	1.31 (126)
	F16	R2	$0.95^{+0.10}_{-0.14}$	$0.28^{+0.04}_{-0.04}$	0.8	1.14 (185)
		D2	$0.99^{+0.11}_{-0.10}$	$0.27^{+0.02}_{-0.02}$	0.8	1.10 (187)
		D3	$0.78^{+0.07}_{-0.12}$	$0.21^{+0.01}_{-0.02}$	0.8	1.16 (195)
		D4	$0.72^{+0.13}_{-0.08}$	$0.15^{+0.01}_{-0.01}$	0.7	1.01 (140)
	F17	...	$0.81^{+0.08}_{-0.08}$	$0.27^{+0.04}_{-0.04}$	0.8	1.05 (190)

Note. LS stands for light curve segments; FS stands for 'flare segments'; N_H is in units of 10^{20} cm^{-2}; temperatures (kT) are in keV; EM is in 10^{52} cm^{-3} and X-ray luminosity (L_X) is in 10^{29} erg s^{-1}. χ^2_ν is the minimum reduced χ^2 and DOF stands for degrees of freedom.
[a]Spectral parameters of hot component in APEC 2T fit.

temperature, loop length and heating rate per unit volume as (Rosner, Tucker & Vaiana 1978; Kuin & Martens 1982)

$$T_{\max} = 1.4 \times 10^3 (pL)^{1/3}, \tag{7}$$

$$E_H \approx 10^{-6} T_{\max}^{3.5} L^{-2} \,\mathrm{erg\,s^{-1}\,cm^{-3}}. \tag{8}$$

The minimum magnetic field necessary to confine the flaring plasma can be simply estimated as

$$B = \sqrt{8\pi p}. \tag{9}$$

Because of limited statistics, we have modelled only 10 flares. The results of the model parameters are listed in Table 8. In this table, column 1 is name of the star and the corresponding flare, column 2 is slope of density–temperature diagram (ζ), column 3 contains loop maximum temperature based on spectral fit and equation (5), semiloop length is determined using the equation (3) and given in column 4, pressure in the loop at the flare peak is estimated using the loop scaling law (see equation 7; column 5), column 6 contains maximum electron density at the flare loop (we have assumed a totally ionized hydrogen plasma, i.e. $p = 2n_e kT_{\max}$; since pressure derived from equation 7 is a maximum value, therefore, a upper limit on density is estimated), volume of the flaring plasma is estimated from maximum EM and from the estimated maximum electron density, and, therefore, is treated as lower limit (equation 6; column 7), column 8 is heating rate per unit volume and estimated using equation (8), the minimum magnetic filed necessary to confine the flaring plasma at loop apex B (see equation 9) is given in column 9, the loop aspect ratio β ($=r/L$, r is radius of the loop cross-section, assuming circular) estimated from the loop scaling law $V = 2\pi\beta^2 L^3$ and number of loops filling the flare volume estimated assuming that $\beta = 0.1$ for a single loop are given in columns 9 and 10, respectively. The model parameters for the different flares from each star are presented and discussed below.

4.5.1 Flares F1, F2 and F4 of V368 Cep

The average temperatures of the loops, usually lower than the real loop maximum temperatures, are found from the spectral analysis of the data as given in Section 4.4. According to equation (5), the loop maximum temperatures for the flare F1, F2 and F4 are found to be 25.5 ± 2.5, 62 ± 8 and 40.3 ± 1.8 MK, respectively. Fig. 11(a) shows the density–temperature (n–T) diagram, where $EM^{1/2}$ has been used as a proxy of density. In Fig. 11(a) the flares F1, F2

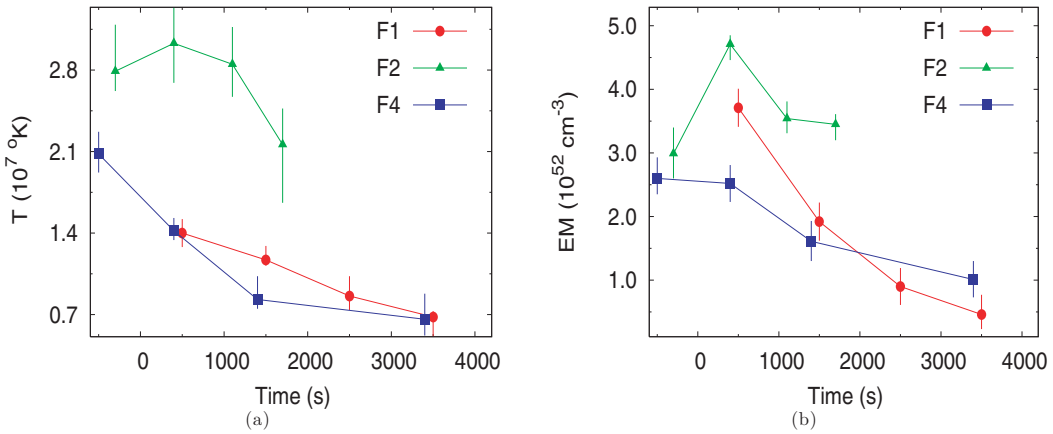

Figure 5. Plots of (a) temperature and (b) EM during the flares F1, F2 and F4 of the star V368 Cep. Here, '0' time corresponds to flare peak and negative scale of time indicates the flare during its rise phase.

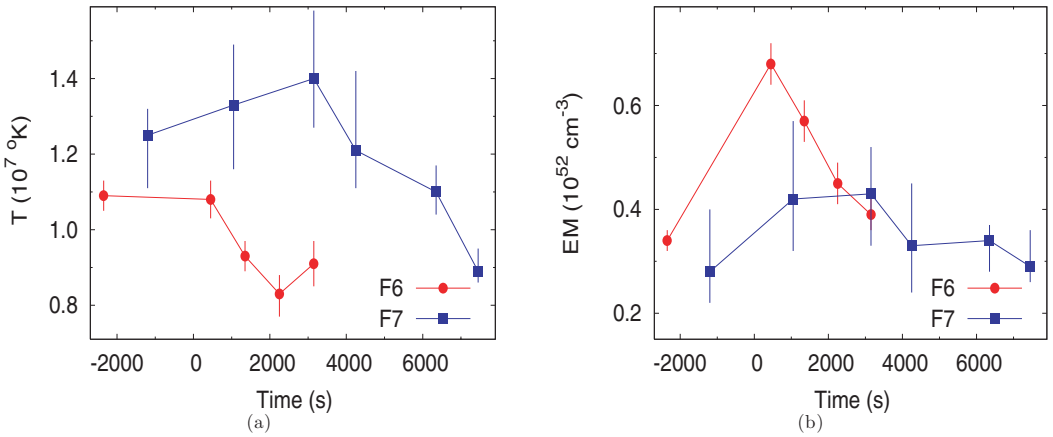

Figure 6. Plots of (a) temperature and (b) EM of dominant component of 2T fit during the flares F6 and F7 of the star XI Boo.

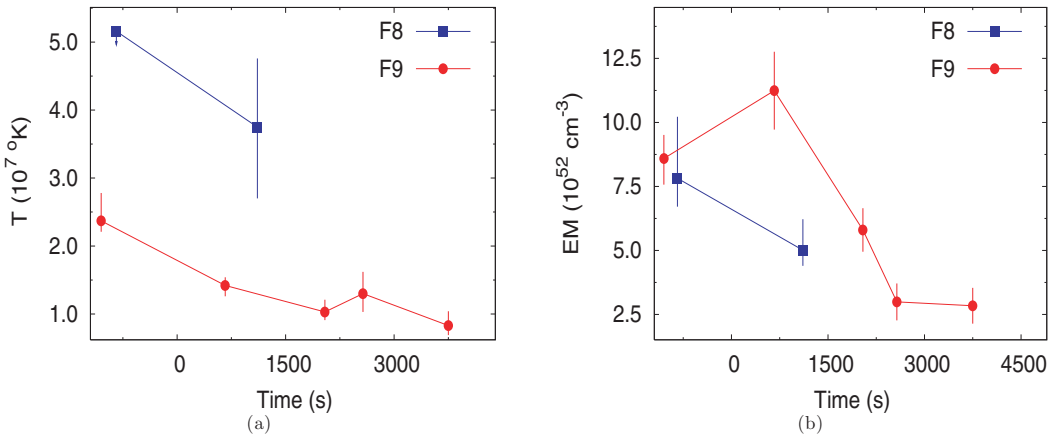

Figure 7. Plots of (a) temperature and (b) EM during the flares F8 and F9 of the star IM Vir. Here arrow shows the upper limit on data point.

and F4 are represented by solid circles, solid triangles and solid squares, respectively. The solid lines represent the best linear fit to the corresponding data, providing the slope ζ. These values of ζ indicate the presence of a sustained heating during the decay of the flares F1 and F2. However, sustained heating is negligible during the decay of the flare F4. As discussed in Section 4.5, the e-folding time of the light curve and the slope of n–T path can be used to estimate the loop half-length. According to equation (3) the semiloop lengths for the flares F1, F2 and F4 are determined to be $6.0 \pm 0.6 \times 10^9$ ($=0.1R_\star$), 19.8 ± 8.6 ($=0.4R_\star$) and $11.7 \pm 1.3 \times 10^9$ ($=0.2R_\star$) cm,

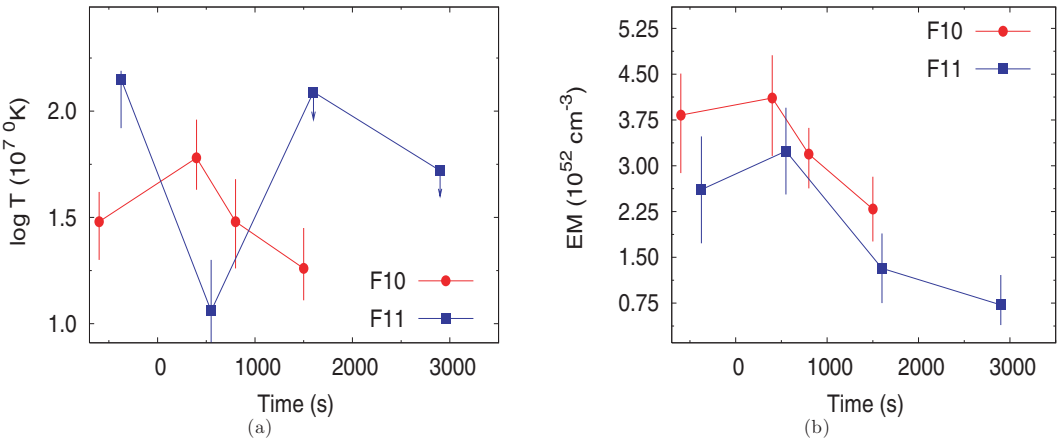

Figure 8. Plots of (a) temperature and (b) EM during the flares F10 and F11 of the star V471 Tau. Here, arrow shows the upper limit on data point.

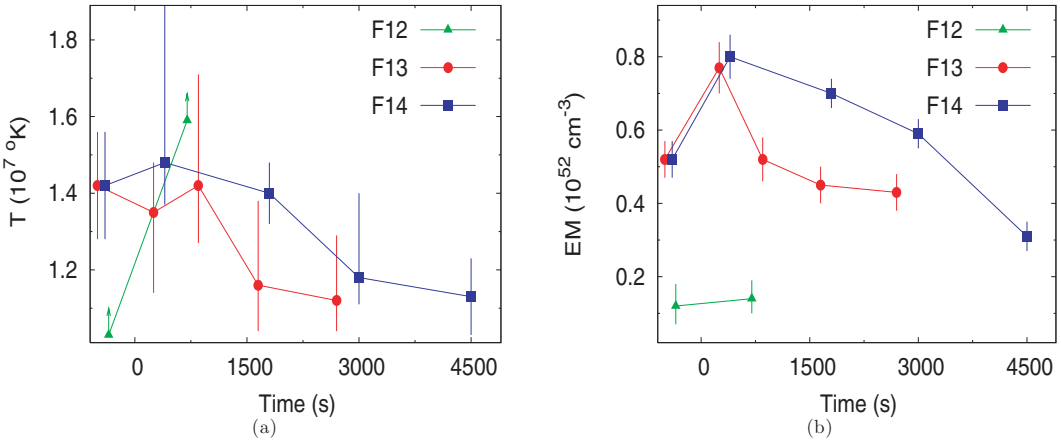

Figure 9. Plots of (a) temperature and (b) EM during the flares F12, F13 and F14 of the star CC Eri. Here, arrow shows the lower limit on data point.

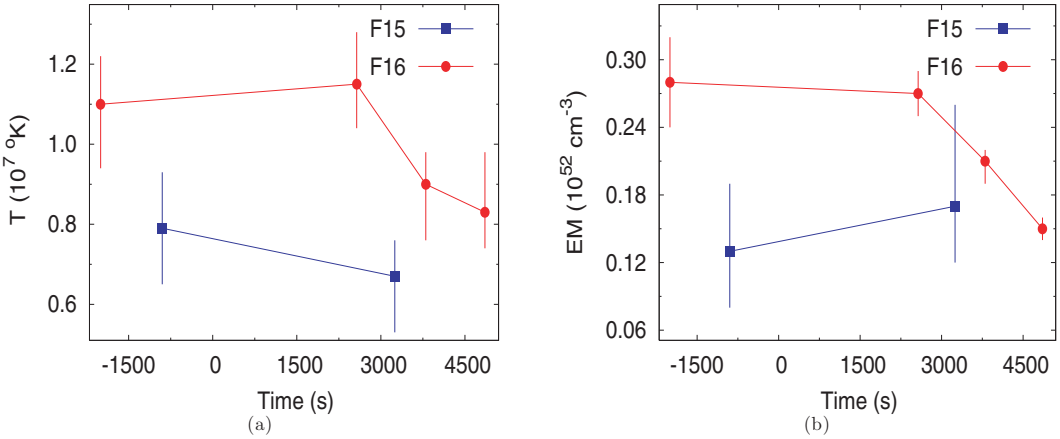

Figure 10. Plots of (a) temperature and (b) EM during the flares F15 and F16 of the star EP Eri.

respectively. These loop lengths are much smaller than the pressure scaleheight[2] $h_p > 1.2 \times 10^{11}$ cm. Maximum pressure in the loop at the flare peak is estimated to be $>10^3$ dyne cm^{-2} for the flares F1, F2 and F4, respectively (see equation 7). Assuming that the hydrogen plasma is totally ionized ($p = 2n_e kT_{max}$), the maximum plasma density in the loop at the flare peak is estimated in the order of 10^{11} cm^{-3} for the flares F1, F2 and F4, respectively. We computed a volume of $\sim 1.78 \times 10^{30}$ cm^{-3} for the flare F1 using the observed peak EM of 3.7×10^{52} cm^{-3}. Similarly, loop volume is determined

[2] Defined as $h_p = 2kT/\mu\ g \sim 5000\, T_{max}/(g/g_\odot)$, where T is plasma temperature in the loop, μ is the molecular weight of the plasmas and g is the surface gravity of the star.

Table 8. Parameters derived for flares.

Object (FN) (1)	ζ (2)	T_{max} (3)	L (4)	p (5)	n_e[a] (6)	V[a] (7)	E_h (8)	B (9)	β (10)	NL (11)
V368 Cep (F1)	0.72 ± 0.03	2.55 ± 0.25	6.0 ± 0.6	1.02 ± 0.32	1.44 ± 0.20	1.78	2.36	160	...	...
V368 Cep (F2)	0.80 ± 0.40	6.20 ± 0.80	19.8 ± 8.6	4.37 ± 2.55	2.56 ± 1.16	0.72	4.75	331	0.12	∼2
V368 Cep (F4)	1.60 ± 0.20	4.03 ± 0.18	11.7 ± 1.3	2.05 ± 0.36	1.84 ± 0.32	0.74	3.06	227	0.27	∼8
XI Boo (F6)	0.73 ± 0.30	1.89 ± 0.08	18.6 ± 7.5	0.13 ± 0.06	0.25 ± 0.10	10.54	0.08	58	0.51	∼26
XI Boo (F7)	2.1 ± 0.4	2.53 ± 0.27	79.4 ± 6.1	0.07 ± 0.02	0.11 ± 0.02	37.81	0.01	43	0.11	∼1
IM Vir (F9)	0.60 ± 0.20	4.66 ± 0.37	18.3 ± 8.9	2.02 ± 1.10	1.57 ± 0.78	4.55	2.07	226	0.34	∼12
V471 Tau (F10)	1.16 ± 0.07	3.35 ± 0.33	21.7 ± 2.5	0.63 ± 0.20	0.68 ± 0.10	8.88	0.46	126	0.37	∼14
CC Eri (F13)	0.51 ± 0.25	2.57 ± 0.29	<14	>0.43	>0.60	<2.15	>0.41	103	0.33	∼11
CC Eri (F14)	0.54 ± 0.15	2.70 ± 0.21	20.0 ± 10.0	0.35 ± 0.20	0.47 ± 0.25	3.60	0.26	95	0.26	∼7
EP Eri (F16)	1.10 ± 0.30	2.02 ± 0.22	23.5 ± 4.5	0.13 ± 0.05	0.23 ± 0.05	5.38	0.07	57	0.26	∼7

(1) FN is flare name.
(2) ζ is slope of decay path in density–temperature diagram.
(3) T_{max} is the maximum temperature in the loop at the flare peak in unit of 10^7 K based on spectral fit and equation (5).
(4) L is half-length of the flaring loop in unit of 10^9 cm and is determined using equation (3).
(5) p is the maximum pressure in the loop at the flare peak in units of 10^3 dyne cm^{-2} (see equation 7).
(6) n_e is the maximum electron density in the loop at the flare peak in unit of 10^{11} cm^{-3}, assuming that hydrogen plasma is totally ionized ($p = 2n_e kT_{max}$).
(7) V is volume of flaring plasma in unit of 10^{30} cm^3 and estimated using the equation (6).
(8) E_h is heating rate per unit volume at the flare peak in the units erg s^{-1} cm^{-3} estimate from the loop scaling laws (see equation 8).
(9) B is minimum magnetic field necessary for confinement in gauss.
(10) β is loop aspect ratio (r/L).
(11) NL is number of loops involve in the flaring plasma.
[a]The pressure as derived from equation (7) is a maximum value, appropriate for the equilibrium condition, which can be reached only for very long-lasting heating. The density and volume values derived thereby are therefore be treated as upper and lower limits, respectively.

to be 7.2×10^{29} cm^3 for flare F2 and 7.4×10^{29} cm^3 for the flare F4. A hint for the heat pulse intensity comes from the flare maximum temperature. By applying the loop scaling laws and loop maximum temperature (see equation 8) the heat pulse intensity for the flares F1, F2 and F4 would be the order of 2.36, 4.75 and 3.06 erg cm^{-3} s^{-1}, respectively. From the pressure of the flare plasma the magnetic field required to confine the plasma should be more than the 160 G for all the flares.

4.5.2 *Flares F6 and F7 of XI Boo*

The evolution of flare F6 and F7 in *n–T* plane is shown in Fig. 11(b), together with a least-square fit to the decay phase. The resulting best-fitting slopes (ζ) for the decaying phase of flare F6 and F7 indicate that the flare F6 is driven by the time-scale of the heating process, whereas sustained heating is negligible during the decay of the flare F7. The intrinsic flare peak temperatures for flare F6 and F7 are, applying equation (5) to the observed maximum temperature, 18.9 ± 0.8 and 25.3 ± 2.7 MK, respectively. For the flare F6 the semiloop length is estimated to be less than the pressure scaleheight, $h_p = 10^{11}$ cm. Maximum pressure and density in the loop at the peak of the flare F6 are estimated to be 130 ± 6 dyne cm^{-2} and $2.5 \pm 1.0 \times 10^{10}$ cm^{-3}, respectively. Using equation (6), volume of the flaring plasma is estimated to be 1.1×10^{31} cm^3. A minimum magnetic field of ∼58 G is required to confine the flaring plasma at the peak of the flare. Although, the value of ζ for the flare F7 is outside the domain of the validity of the method (see Reale 2007), the estimated loop parameters obtained from the hydrodynamic loop modelling are listed in Table 8. The estimated semiloop length for the flare F7 is smaller than the pressure scaleheight (=1.3×10^{11} cm).

4.5.3 *Flare F9 of IM Vir*

Using equation (5) the maximum loop temperature for the flare F9 is found to be 46.6 ± 3.7 MK. Fig. 11(c) shows the *n–T* diagram for the flare F9. From the best linear fit, we found the slope of the *n–T* diagram implies that the heating during the flare decay was as strong as in the flares F1, F2 and F6. The resulting semiloop length is found to be 10 times smaller than the pressure scaleheight ($h_p = 2.3 \times 10^{11}$ cm), which implies a loop in hydrostatic equilibrium with a plasma pressure of 2020 ± 1100 dyne cm^{-2} and maximum heating rate of ≈2.07 erg cm^{-3} s^{-1}. The maximum plasma density and loop volume for the flare are estimated to be $1.6 \pm 0.8 \times 10^{11}$ and 4.55×10^{30} cm^3, respectively. The minimum confining magnetic field is estimated to be ∼226 G.

4.5.4 *Flare F10 of V471 Tau*

The maximum temperature in the loop at the flare peak was found to be 33.5 ± 3.3 MK for the flare F10 (see Fig. 11d for the *n–T* diagram of this flare). The slope of the decay path of *n–T* diagram indicates the presence of sustained heating. Using equation (3) the semiloop length of the flare F10 is calculated to be $\sim 0.4 R_\star$ and is ∼five times smaller than the pressure scaleheight $h_p = 1.2 \times 10^{11}$ cm. Using these parameters and the scaling laws for the loops, the maximum pressure, the maximum density and the minimum magnetic field confining the flaring plasma in the loop at the flare peak, the volume of flaring plasma and the heating rate per unit volume for F10 are estimated to be $p = 630 \pm 200$ dyne cm^{-2}, $n_e = 6.8 \pm 1.0 \times 10^{10}$ cm^{-3} and $B = 126$ G, 8.9×10^{30} cm^3 and 0.46 erg s^{-1} cm^{-3}.

4.5.5 *Flares F13 and F14 of CC Eri*

Using equation (5) the maximum temperature in the loop responsible for the flares F13 and F14 are found to be 25.7 ± 2.9 and 27.0 ± 2.1 MK, respectively. Fig. 11(e) shows the *n–T* diagram for these flares. The slopes in *n–T* diagram for the flares F13 and F14

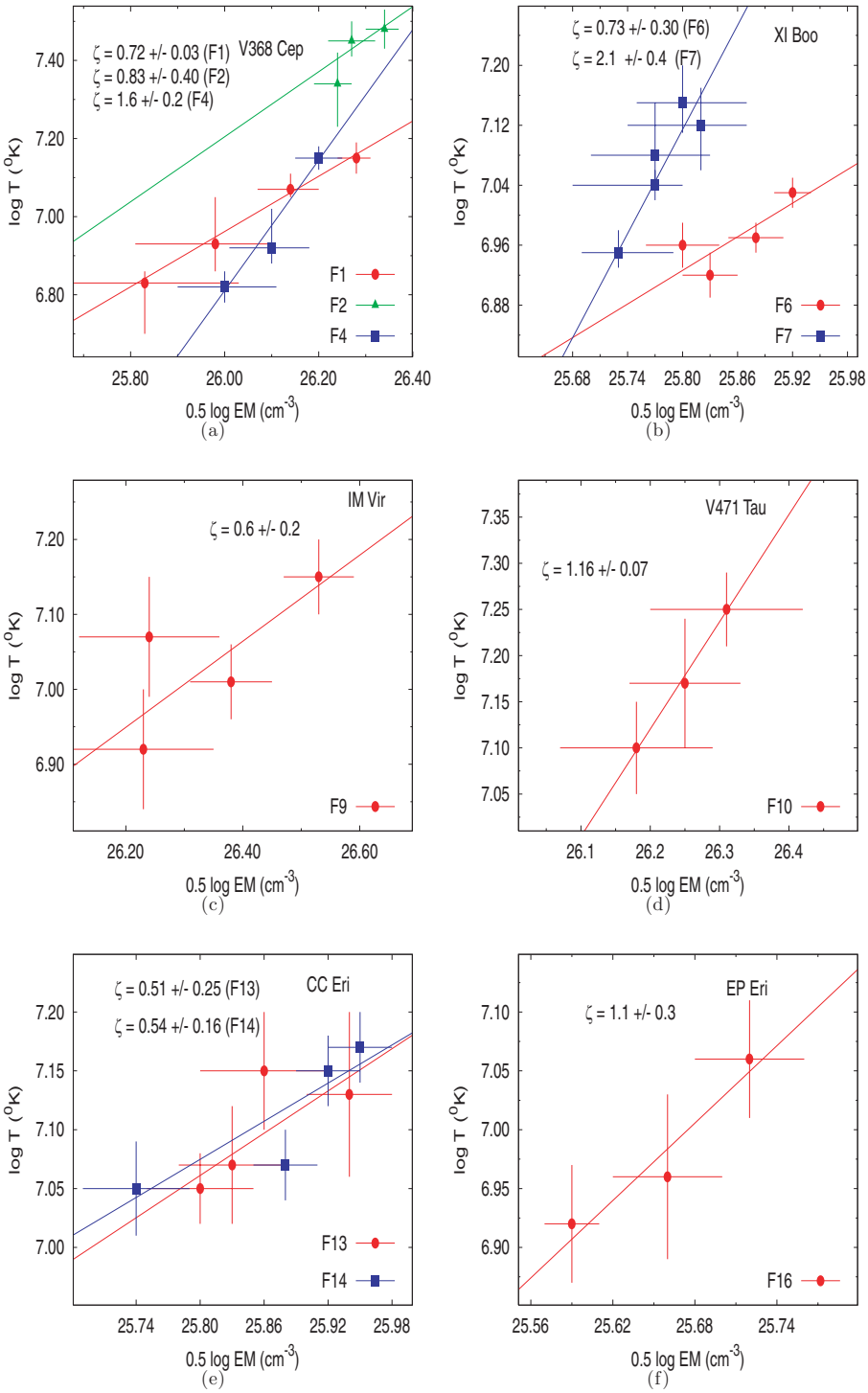

Figure 11. The density–temperature diagram, where $EM^{1/2}$ has been used as a proxy of density. Symbols for the each flare are given at the bottom right-hand corner. Straight lines represent the best linear fit to the corresponding data. ζ is slope of density–temperature diagram.

indicate the presence of strong sustained heating, and showing that the observed decay is driven by the time evolution of the heating process. The value of ζ at the low extreme of the error bar for the flare F13 is compatible with the lower asymptotic value for which equation (4) can be applied. Therefore, an upper limit for semilength of the loop can be derived by using the value of ζ at the high extreme of the error bar. The resulting semilength for the flares F13 and F14 are $<1.4 \times 10^{10}$ (=0.3/0.5 $R_\star$) and $2.0 \pm 1.0 \times 10^{10}$ (=0.4/0.7 $R_\star$) cm, respectively. These values of the loop length are much smaller than the pressure scaleheight $h_p = 1.1 \times 10^{11}$ cm for flare F13 and $h_p = 7.3 \times 10^{10}$ cm for flare F14. A magnetic field more than 95 G is required to confine the flaring plasma at the top of both flares. A detailed analysis of these flares is also given in Crespo-Chacon et al. (2007). The estimated loop parameters for both flares are found well within 1σ level to that of Crespo-Chacon et al. (2007).

4.5.6 Flare F16 of EP Eri

The trend in *n–T* diagram suggests the presence of significant heat during the decay of the flare F16 (see Fig. 11f and Table 8). The temperature at the peak of the flare is determined to be 20.2 ± 2.2 MK. The derived semiloop length $L = 2.4 \pm 0.5 \times 10^{10}$ cm ($=0.4R_\star$) is less than the pressure scaleheight $h_p = 9 \times 10^{10}$ cm. Using the same approach as discussed above, the maximum pressure and the maximum density are derived at $p = 130 \pm 50$ dyne cm^{-2} and $n_e = 2.3 \pm 0.5 \times 10^{10}$ cm^{-3}. Using the maximum EM, the loop volume is estimated to be 5.38×10^{30} cm^3. The confining magnetic filed is estimated as $B > 57$ G.

5 DISCUSSION AND CONCLUSIONS

We have carried out an analysis of *XMM–Newton* observations of six G–K dwarfs. Light curves revealed flaring in all the stars on time-scale ranging from seconds to kiloseconds, with various peak strengths. A total of 17 flares were identified in these G–K dwarfs. The decay time of these flares ranges from 0.5 to 10 ks. A similar range of flare decay times in the pre-main-sequence stars of Pleiades cluster was found by Stelzer, Neuhäuser & Hambaryan (2000). Among the 17 flares presented here, only four flares (F6 and F7 of XI Boo, F9 of IM Vir and F14 of CC Eri) appear to be long decay flare ($\tau_d \geqslant 1$ h). In fact, the flare F7 of XI Boo was one of the longest duration flares observed with $\tau_d \sim 10$ ks. Such long decay flares have so far been reported in CF Tuc ($\tau_d = 79.2$ ks; Kürster & Schmitt 1996), EV Lac ($\tau_d = 37.8$ ks; Schmitt 1994), Algol ($\tau_d = 30.2$ ks; Ottmann & Schmitt 1996), AD Leo ($\tau_d = 7.9$ ks; Favata et al. 2000b) and some pre-main-sequence stars (Stelzer et al. 2000; Favata et al. 2005). This flare classification is purely based on the decay time. It has been shown that even much longer flares can occur in a single loop (Favata et al. 2005), while relatively short flares with heating dominated decay are probably arcade flares. For the flares F6, F9 and F14, the decay path is driven by the sustained heating, therefore, these flares cannot be classified as long decay flares. However, the sustained heating during the decay of the flare F7 is negligible. Thus, these flares can be classified as arcade. The flare decay time for the remaining 12 flares is similar to that of the solar compact flares. The morphological differences in these different types of flares indicate the different processes of energy released. In compact flares energy is probably released only during an impulsive phase, whereas in the two-ribbon flares a prolonged energy release is apparently required to explain their long decay time (Pallavicini, Serio & Vaiana 1977; Priest 1981; Pallavicini et al. 1988; Poletto, Pallavicini & Kopp 1988). The rise time of these flares has been found to be less than 1 ks, which is similar to the rise time of impulsive flares observed in the M dwarfs (Pallavicini et al. 1990). However, for some flares (F6, F7 and F9) the rise time was found to be more than 1 ks. We found that the decay times of the flares observed here are more in the soft band than in the medium band or the hard band. Some flares, e.g. F2, actually showed a hard peak during the decay. However, even then the τ_d in soft band being more than in the hard band. This could probably be due to the softening of the spectrum during the decay due to the plasma cooling i.e. emission gradually exists form high energy band and enters more deeply in the soft energy band or the higher energy electrons streaming down from the coronal heights to the chromosphere that can heat the plasma to higher temperature, lose their energy faster than the lower energy electrons. Most of the flares observed in our sample were found to have more peak flux in the soft band than in the medium and hard band.

The total energy released during the X-ray flares observed in the sample of G–K dwarfs is observed to be in the range of 2.3×10^{32} to 6.1×10^{34} erg. This shows that these flares are 10 times more energetic than the flares in the M-type dwarfs (Pallavicini et al. 1990), and 10^2 to 10^4 times more energetic than the solar flares (Moore et al. 1980; Wu et al. 1986). However, they are not as energetic as a large flare observed in Algol ($E_{tot} = 10^{35}$ erg; White et al. 1986), but are as energetic as the flares observed in G9 dwarf ZS 76 ($E_{tot} = 1.4 \times 10^{34}$ erg; Pillitteri et al. 2005). The large flare, F7, of XI Boo was the largest in terms of both the decay time and the ratio of the peak luminosity to the quiescent luminosity (a factor of 2.2). However, given the low quiescent emission ($L_X = 5.1 \times 10^{28}$ erg s^{-1}) from the XI Boo, this flare was not particularly prominent in terms of either peak X-ray luminosity ($L_X = 1.1 \times 10^{29}$ erg s^{-1}) or the total X-ray energy ($E_{tot} = 6.4 \times 10^{33}$ erg). Other large flare F9 of IM Vir shows a large peak X-ray luminosity (1.6×10^{30} erg s^{-1}) as well as the total energy released ($E_{tot} = 6.12 \times 10^{34}$ erg).

In spite of the fact that the peak flare luminosity may vary by a factor of 2 (see e.g. IM Vir in Table 7), there is a good correlation between the peak flare luminosities (L_{Xf}) and the quiescent state stellar X-ray luminosities (L_{Xq}). The form of the correlation is $\log L_{Xf} = 1.04 \log L_{Xq} + 1.3$, with the correlation coefficient, *r*, of 0.9 (see Fig. 12). A similar correlation was found by Pallavicini et al. (1990) for the M dwarfs. This indicates that there is a direct connection between the flaring and the quiescent X-ray emission, which is probably due to their common emission mechanism for X-rays.

Flares F2–F3–F4, F6–F7 and F10–F11 show the similar structure i.e. before ending the first flare the next flare starts. Similar loop systems have been observed to the flare on the Sun (e.g. so-called Bastille Day flare; Aschwanden & Alexander 2001), and in a stellar analogue dMe star Proxima Centauri (Reale et al. 2004). In these two events, a double ignition in nearby loops was observed or suggested, and the delay between the ignitions appears to scale with the loop sizes. Similar type of double exponential decay was also found

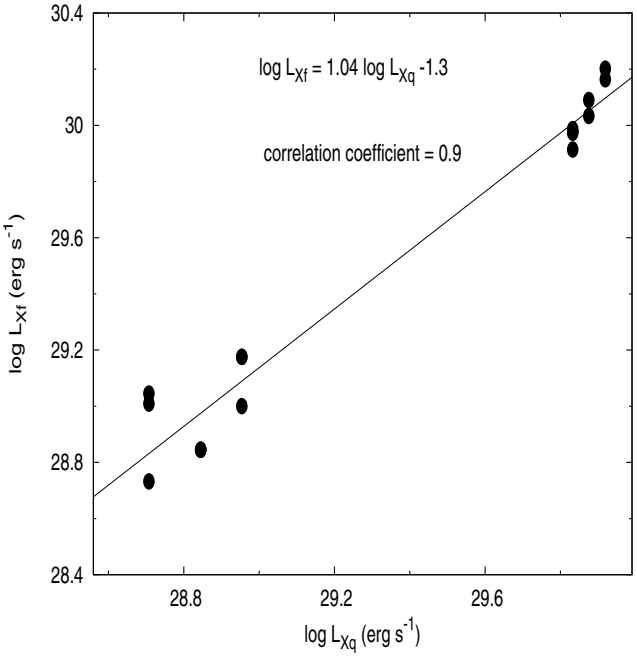

Figure 12. Plot of peak flare luminosity (L_{Xf}) versus stellar quiescent luminosity (L_{Xq}).

in the young stars ZS 76 (Pillitteri et al. 2005) and Cygnus OB2 (Albacete Colombo et al. 2007). This implies that in these dwarfs a steady active region undergoes a strong magnetic reconnection event resulting in an intense flare, and is followed by an arcade of reconnected loops that slowly decay.

We have performed time resolved spectroscopy of these flares. The coronal spectrum during the flare can be represented with a 1T model, with quiescent state taken into account as a frozen background contribution. During the flares F1, F9 and F11 the EM was increased by a factor of 5 or more. Such large variation in EMs was also seen during the flares detected in AB Dor (Maggio et al. 2000). Both the temperature and EM show the well-defined trends i.e. the changes in the temperature and the EM are correlated with the variations observed in the light curves during the flares. Similar trends were also seen during the flares detected in the pre-main-sequence stars of the Orion Nebula cluster (Favata et al. 2005) and star-forming complex L1551 in Taurus (Giardino et al. 2006). Reale, Peres & Orlando (2001) found that the height of EM distributions are variable during the different phases of the solar flares, while its width and the peak temperature of the distribution undergo much smaller changes. The peak flare temperature is found in the range of 20–60 MK for all the flares. These values are intermediate between those of flares observed on active stars like Algol ($T_{\rm max} \sim$ 100–150 MK; Favata et al. 2000c), AB Dor ($T_{\rm max} \sim$ 140–170 MK; Maggio et al. 2000), those found in flares on the dMe star AD Leo (range 20–50 MK; Reale & Micela 1998; Favata et al. 2000b), on solar-type Pleiades (20–40 MK; Briggs & Pye 2003) and young stellar objects ($T_{\rm max} \sim$ 80–270 MK; Favata, Micela & Reale 2001; Favata et al. 2005). For most of flares both EM and temperature peaked simultaneously. However, for few flares (F9, F11, F13), it appears that the temperature was evolved before the EM. Similar delay is often observed both in solar flare (Sylwester et al. 1993) and in flares from the stars Algol (van den Oord & Mewe 1989), EV Lac (Favata et al. 2000b), AB Dor (Maggio et al. 2000) and YY Gem (Stelzer et al. 2002). This is probably due to an impulsive flare event, in which loop does not reach equilibrium conditions, the density begins to decay later than the temperature.

We have modelled the flares using the hydrodynamic model (see Section 4.5; Reale et al. 1997) based on the decay phase of the flare. The derived semiloop lengths for all flares are found to be in the range of 0.6–8.0 $\times$ 10^{10} cm. Alternatively, Reale (2007) derive the semiloop length from the rise phase and peak phase of the flare as

$$L'_9 \approx 3\psi^2 T_{\rm max}^{1/2} t_{\rm M}, \tag{10}$$

where L'_9 is semiloop length in the unit of 10^9 cm, $\psi = T_{\rm max}/T_{\rm M}$, $T_{\rm max}$ is maximum temperature in the unit of 10^7 K, $T_{\rm M}$ is temperature at density maximum and $t_{\rm M}$ is time in the unit of 10^3 s at which density maximum occurs. The time of the maximum EM is a good proxy for $T_{\rm M}$. In case where both temperature and EM were simultaneously peaked during the rise phase, only rise time was used in the estimation of the semiloop length. The semiloop lengths estimated from this approach for the flares F4 ($L'_9 = 13.6 \pm 3.2$ cm), F6 ($L'_9 = 16.8 \pm 1.8$ cm), F13 ($L'_9 = 6.6 \pm 1.4$ cm), F14 ($L'_9 = 11.4 \pm 3.1$ cm) and F16 ($L'_9 = 20.8 \pm 5.8$ cm) are found to be consistent with that of estimated from the decay phase analysis (see also Table 8). The estimated loop length, L'_9, for the flares F2 (9 ± 2 cm), F7 (36 ± 8 cm) and F10 (7 ± 2 cm) are found to be less than that of determined from decay phase. However, for the flare F9 of IM Vir the estimated loop length ($L'_9 = 41 \pm 13$ cm) is two times more than that of estimated from decay phase. The inconsistency in the estimation of the loop length from the two approaches is probably due to the involvement of other different coronal loops during the decay of the flare or the heat pulse triggering the flare is not a top-hat function. This new analysis allows us to derive the loop lengths of the flares for which either time resolved spectral information is not available or decay phase is not observed. These flares are F11 of V471 Tau, and F15 and F17 of EP Eri. The estimated semiloop lengths for these flares F11, F15 and F17 are 6.2 $\times$ 10^{10}, 2.1 $\times$ 10^{10} and 3.8 $\times$ 10^9 cm, respectively. Therefore, the magnetic structures confining the plasma for all the observed flares in G–K dwarfs are smaller than the star themselves, and are not as large as observed in a single giant HR 9024 ($L = R_\star/2$; Testa et al. 2007) and some pre-main-sequence analogues ($L \gg R_\star$; Favata et al. 2005; Giardino et al. 2006).

For all the flares, the estimated maximum electron density under assumption of a totally ionized hydrogen plasma is found in the order of 10^{10-11} cm^{-3}. This is compatible with the values expected for the plasma in coronal condition (Landini et al. 1986). To satisfy the energy balance relation for the flaring as a whole, the maximum X-ray luminosity must be lower than the total energy rate ($H = E_{\rm H} \,.\, V$; see Section 4.5) at the flare peak. The rest of the input energy is used for thermal conduction, kinetic energy and radiation at lower frequencies. For the flares F2 and F4 of V368 Cep the maximum X-ray luminosity observed is about 34 per cent of H. Similarly, for the flares F7 of XI Boo and F10 of V471 Tau the maximum X-ray luminosity is about 30 per cent of H. However, for other flares (see Table 7) only 16–22 per cent of H is observed as a peak luminosity. These values are in agreement with those reported for the solar flares, where the soft X-ray radiation only accounts for up to 20 per cent of total energy (Wu et al. 1986). In comparison, the fraction of X-ray radiation to the total energy has been found to be 15 and 35 per cent for the M dwarfs Proxima Centauri and EV Lac, respectively (Favata et al. 2000a; Reale et al. 2004). Applying loop scaling law $V = 2\pi\beta^2 L^3$, and if the detected flares are produced by a single loop, their aspect ratio (β) were estimated in the range of 0.1 to 0.3 for the flares F2, F4, F7, F9, F13, F14 and F16 (see Table 8). Similar cross-section was also observed for the solar coronal loops for which typical values of β are in the range of 0.1–0.3. If we assume $\beta = 0.1$, these flares occurred in the arcades, which are composed of two to 11 loops (see also Table 8). However, for the flares F6 and F10 the value of β (assuming single loop) is estimated to be 0.51 and 0.37, respectively. In comparison to the solar coronal loops, the cross-section for these flare loops is very large. It appears that the flares F6 and F10 occurred in the arcades that contain 26 and 14 loops, respectively.

Therefore, we conclude that the observed flares in G–K dwarfs are similar to the solar arcade flares, which are as strong as M dwarfs and are much smaller than the flare observed in dMe star, giants and pre-main-sequence analogous.

ACKNOWLEDGMENTS

We thank the reviewer of the paper for very useful comments and suggestions. This research has made use of data obtained from HEASARC, provided by the NASA Goddard Space Flight Center.

REFERENCES

Albacete Colombo J. F., Caramazza M., Flaccomio E., Micela G., Sciortino S., 2007, A&A, 474, 495

Anders E., Grevesse N., 1989, Geochim. Cosmochim. Acta, 53, 197

Arnaud K. A., 1996, in Jacoby G. H., Barnes J., eds, ASP Conf. Ser. Vol. 101, Astronomical Data Analysis Software and Systems V. Astron. Soc. Pac., San Francisco, p. 17

Aschwanden M. J., Alexander D., 2001, Sol. Phys., 204, 91
Ayres T. R., Marstad N. C., Linsky J. L., 1981, ApJ, 247, 545
Baliunas S. L. et al., 1995, ApJ, 438, 269
Briggs K. R., Pye J. P., 2003, MNRAS, 345, 714
Cayrel de Strobel G., Cayrel R., 1989, A&A, 218, 9
Chugainov P. F., Lovkaya M. N., Petrov P. P., 1991, Inf. Bull. Var. Stars, 3623
Chugainov P. F., Petrov P. P., Lovkaya M. N., 1993, Izv. Krym. Astrofiz. Obs., 88, 29
Crespo-Chacon I., Micela G., Reale F., Caramazza M., Lopez-Santiago J., Pilleteri I., 2007, A&A, 471, 929
Cutispoto G., 1992, A&AS, 95, 397
Dennis B. R., Schwartz R. A., 1989, Sol. Phys., 121, 75
Dickey J. M., Lockman F. J., 1990, ARA&A, 28, 215
Ehle M. et al., 2004, User's Guide to XMM–Newton Science Analysis System. Available at http://xmm.vilspa.esa.es
Favata F., Reale F., Micela G., Sciortino S., Maggio A., Matsumoto H., 2000a, A&A, 353, 987
Favata F., Micela G., Reale F., 2000b, A&A, 354, 1021
Favata F., Micela G., Reale F., Sciortino S., Schmitt J. H. M. M., 2000c, A&A, 362, 628
Favata F., Micela G., Reale F., 2001, A&A, 375, 485
Favata F., Flaccomio E., Reale F., Micela G., Sciortino S., Shang H., Stassun K. G., Feigelson E. D., 2005, ApJS, 160, 469
Fekel F. C., 1997, PASP, 109, 514
Garcia-Alvarez D., 2000, Ir. Astron. J., 27, 117
Garcia-Alvarez D., Jevremovic D., Doyle J. G., Butler C. J., 2002, A&A, 383, 548
Giardino G., Favata F., Silva B., Micela G., Reale F., Sciortino S., 2006, A&A, 453, 241
Gray D., Baliunas S., Lockwood G., Skiff B., 1996, ApJ, 465, 945
Güdel M., 2004, ARA&A, 12, 71
Guinan E. F., Sion E. M., 1984, AJ, 89, 1252
Haisch B. M., Linsky J. L., Bornmann P. L., Stencel R. E., Antiochos S. K., Golub L., Vaiana G. S., 1983, ApJ, 267, 280
Hartmann L., Schmidtke P. C., Davis R., Dupree A. K., Raymond J., Wing R. F., 1979, ApJ, 233, L69
Hawley S. L. et al., 1995, ApJ, 453, 464
Henry G. W., Fekel F. C., Hall D., 1995, AJ, 110, 2926
Hoffleit D., Jaschek C., 1982, The Bright Star Catalogue, 4th edn. Yale Univ. Obs., New Haven, CT
Jansen F. et al., 2001, A&A, 365, L1
Johns-Krull C. M., Valenti J. A., 1996, in Pallavicini R., Dupree A. K., eds, ASP Conf. Ser. Vol. 109, Cool Stars, Stellar Systems, and the Sun. Astron. Soc. Pac., San Francisco, p. 609
Kopp R. A., Poletto G., 1984, Sol. Phys., 93, 351
Kuin N. P. M., Martens P. C. H., 1982, A&A, 108, 1
Kürster M., Schmitt J. H. M. M., 1996, A&A, 311, 211
Laming J. M., Drake J. J., 1999, ApJ, 516, 324
Landini M., Monsignori Fossi B. C., Pallavicini R., Piro L., 1986, A&A, 157, 217
Maggio A., Pallavicini R., Reale F., Tagliaferri G., 2000, A&A, 356, 627
Malkov O. Y., Oblak E., Snegireva E. A., Torra J., 2006, A&A, 446, 785
Moore R. et al., 1980, in Sturrock P. A., ed., Solar Flares. Colorado Assoc. Univ. Press, Boulder, CO, p. 341
Nelson B., Young A., 1970, PASP, 82, 699
Olah K., Strassmeier K. G., 2002, Astron. Nachr., 323, 361
Ottmann R., Schmitt J. H. M. M., 1996, A&A, 307, 813
Pallavicini R., Serio S., Vaiana G. S., 1977, ApJ, 216, 108
Pallavicini R., Monsignori-Fossi B. C., Landini M., Schmitt J. H. M. M., 1988, A&A, 191, 109
Pallavicini R., Tagliaferri G., Stella L., 1990, A&A, 228, 403
Pillitteri I., Micela G., Reale F., Sciortino S., 2005, A&A, 430, 155
Poletto G., Pallavicini R., Kopp R. A., 1988, A&A, 201, 93
Priest E. R., 1981, in Priest E. R., ed., Solar Flare Magnetohydrodynamics. Gordon & Breach, New York, p. 1
Reale F., 2002, in Favata F., Drake J. J., eds, ASP Conf. Ser. Vol. 277, Stellar Coronae in the Chandra and XMM-Newton Era. Astron. Soc. Pac., San Francisco, p. 103
Reale F., 2007, A&A, 471, 271
Reale F., Micela G., 1998, A&A, 334, 1028
Reale F., Betta R., Peres G., Serio S., McTiernan J., 1997, A&A, 325, 782
Reale F., Peres G., Orlando S., 2001, ApJ, 557, 906
Reale F., Güdel M., Peres G., Audard M., 2004, A&A, 416, 733
Rosner R., Tucker W. H., Vaiana G. S., 1978, ApJ, 220, 643
Saar S. H., 1990, in Stenflo J. O., ed., Proc. IAU Symp. 138, The Solar Protosphere: Structure, Convection, and Magnetic Fields. Kluwer, Dordrecht, p. 427
Schimtt J. H. M. M., 1994, ApJS, 90, 735
Schimtt J. H. M. M., 1997, A&A, 318, 215
Schimtt J. H. M. M., Favata F., 1999, Nat, 401, 44
Serio S., Reale F., Jakimiec J., Sylwester B., Sylwester J., 1991, A&A, 241, 197
Smith R. K., Brickhouse N. S., Liedahl D. A., Raymond J. C., 2001, ApJ, 556, L91
Stelzer B., Neuhäuser R., Hambaryan V., 2000, A&A, 356, 949
Stelzer B. et al., 2002, A&A, 392, 585
Strassmeier K. G., Hall D. S., Fekel F. C., Scheck M., 1993, A&AS, 100, 173
Strüder L. et al., 2001, A&A, 365, L18
Sylwester B., Sylwester J., Serio S., Reale F., Bentley R. D., Fludra A., 1993, A&A, 267, 586
Testa P., Reale F., Garcia-Alvarez D., Huenemoerder P., 2007, ApJ, 663, 1232
Turner M. J. L. et al., 2001, A&A, 365, L27
van den Oord G. H. J., Mewe R., 1989, A&A, 213, 245
White N. E., Culhane J. L., Parmar A. N., Kellett B. J., Kahn S., van den Oord G. H. J., Kuijpers J., 1986, ApJ, 301, 262
Wu S. T. et al., 1986, in Kundu M., Woodgate B., eds, NASA Conf. Publ. 2439, Energitic Phenomenon on the Sun. NASA, Washington, DC, p. 5

This paper has been typeset from a TEX/LATEX file prepared by the author.